Evolution of the velocity-gradient tensor in a spatially developing turbulent flow

R. Gomes-Fernandes[1]**B. Ganapathisubramani** [2]
and J. C. Vassilicos[1]

[1]Department of Aeronautics, Imperial College London, London SW7 2AZ, UK
[2]Aerodynamics & Flight Mechanics Research Group, University of Southampton, Southampton SO17 1BJ, UK

(Received ?; revised ?; accepted ?. - To be entered by editorial office)

An experimental study of turbulence generated by a low-blockage space-filling fractal square grid was performed using cinematographic stereo particle image velocimetry in a water tunnel. All fluctuating velocity gradients were measured and their statistics were computed at three different stations along the streamwise direction downstream of the grid: in the production region, at the location of peak turbulence intensity and in the non-equilibrium decay region. The usual signatures of these statistics are only found in the decay region where a well-defined 2/3 power-law dependence of the second order structure function on two-point distance is also present. However this 2/3 exponent is well defined over a wide range of scales even at the peak location where the statistics of the fluctuating velocity gradient tensor are very unusual. There, as at the production region station, the $Q-R$ tear-drop shape is not yet fully developed, vortex stretching only slightly dominates over compression and they both very widely fluctuate reaching very high low-probability values. In these two stations there is also only marginal preference between sheet-like and tube-like velocity gradient structures as seen by the sign of the second eigenvalue of the strain rate tensor. Yet, there are subregions of the flow in the production region where the 2/3 exponent is present and where the $Q-R$ tear drop shape is as undeveloped as for the entire data set at this station.

1. Introduction

As demonstrated by Simmons & Salter (1934) and Jayesh & Warhaft (1992) for regular grids, by Hurst & Vassilicos (2007) for fractal square grids and by Krogstad & Davidson (2012) for fractal (multi-scale) cross grids, the turbulence generated by such grids when they are obstructing a laminar free stream is characterised by two regions. One closest to the grid where the turbulence is being produced and mostly increases with downstream distance (the production region) and an adjacent subsequent region where the turbulence decays with distance downstream (the decay region). The overwhelming majority of the research work on grid-generated turbulence to date has concentrated on the decay region. Over the past six years evidence has accumulated (Seoud & Vassilicos 2007; Mazellier & Vassilicos 2010; Valente & Vassilicos 2011, 2012; Gomes-Fernandes *et al.* 2012; Discetti *et al.* 2013; Nagata *et al.* 2013) that a near-field sub-region of the decay region exists in the lee of both fractal and regular grids where (i) the energy spectrum has a well-defined -5/3 power-law spectrum over a wide range of wavenumbers, (ii) the fluctuating velocities are approximately Gaussian, (iii) the mean flow and turbulence intensity profiles are only weakly inhomogeneous or approximately homogeneous yet (iv) the dimensionless dissipation coefficient, $C_\epsilon \equiv \epsilon L/u'^3$ is not constant but varies with Reynolds numbers $Re_I = U_\infty L_b/\nu$ and $Re_\lambda = u'\lambda/\nu$ as $C_\epsilon \propto Re_I/Re_\lambda$ (ϵ is the turbulent kinetic energy dissipation rate per unit mass, u' is the root mean square (r.m.s.) of the streamwise velocity fluctuation, L is an integral length scale, U_∞ is the free stream velocity upstream of the grid, L_b is a length-scale characterising the grid, λ is the Taylor microscale and ν is the kinematic viscosity). Tennekes & Lumley (1972) refer to $C_\epsilon = Const$ as "one of the cornerstone assumptions of turbulence theory"; in particular it is part and parcel of the Richardson-Kolmogorov equilibrium cascade (Kolmogorov 1941*b*,*c*,*a*; Batchelor 1953) which implies a $-5/3$ power-law energy spectrum. The relation $C_\epsilon \propto Re_I/Re_\lambda$ therefore characterises non-equilibrium turbulence and the existence of a well-defined -5/3 power-law energy spectrum in such turbulence cannot be explained by usual Kolmogorov arguments.

These observations raise the following questions: (i) could it be that the -5/3 spectrum and its equivalent 2/3 power-law shaped second order structure function are already present in the production region as suggested by the Direct Numerical Simulations (DNS) of Laizet *et al.* (2013)? (ii) The turbulent kinetic energy dissipation being directly related to the fluctuating velocity gradients, does the new non-equilibrium dissipation law $C_\epsilon \propto Re_I/Re_\lambda$ imply unusual statistics of these small-scale gradients? (iii) How do these statistics evolve from production to decay regions? (iv) How does the shape of the second order structure function correlate with these statistics?

The fluctuating velocity gradient tensor is characterised by three invariant quantities P, Q and R which are independent of the orientation of the coordinate system and provide information about the local topology of the turbulence. The first invariant P is zero for incompressible flows, hence the majority of studies have concentrated on Q and R. The joint PDF of Q and R (referred to as $Q-R$ diagram) appears to have a tear-drop shape universal to many turbulent flows (see Tsinober 2009). Another acclaimed universal feature of small-scale turbulence concerns the statistics of alignments between the vorticity and the principal directions of the strain rate tensor. In three-dimensional incompressible flows the principal directions consist of one extensive and one compressive direction and an intermediate direction which can, a priori, be either extensive or compressive. The usual small-scale turbulence behaviour, assumed universal (see Tsinober 2009), is that vorticity is preferentially aligned with the intermediate direction, misaligned with the compressive direction and more or less indifferent as to the orientation of the extensive direction. Betchov (1956) showed that the forward cascade of turbulent kinetic energy requires that this intermediate direction be weakly extensive implying a universal asymmetry between compressive and extensive strain rates. The -5/3 and 2/3 exponents of the energy spectrum and second order structure functions being seen as universal features of small-scale turbulence, it is natural to ask how they correlate with the presumed universal statistics of the fluctuating velocity gradients and how they develop, together or separately, in a spatially developing flow such as grid-generated turbulence (see Laizet *et al.* 2013).

To the best of the authors' knowledge the only study to date of the concurrent spatial evolution of fluctuating velocity gradient statistics and the second order structure function is the DNS study of Laizet *et al.* (2013). Their DNS study was of turbulence generated by a fractal square grid where the production and the non-equilibrium decay regions are much longer than in the lee of usual regular grids yet the flow remains approximately homogeneous (or weakly inhomogeneous) around the centreline in the decay region. Fractal square grids are therefore a good choice of grid if it is desired to resolve the production and non-equilibrium decay regions. In this paper we present an experimental study of fluctuating velocity gradient statistics and of the second order structure function at three locations downstream of a space-filling fractal square grid, one in the production region, one at the peak of turbulence intensity (which demarcates the production and

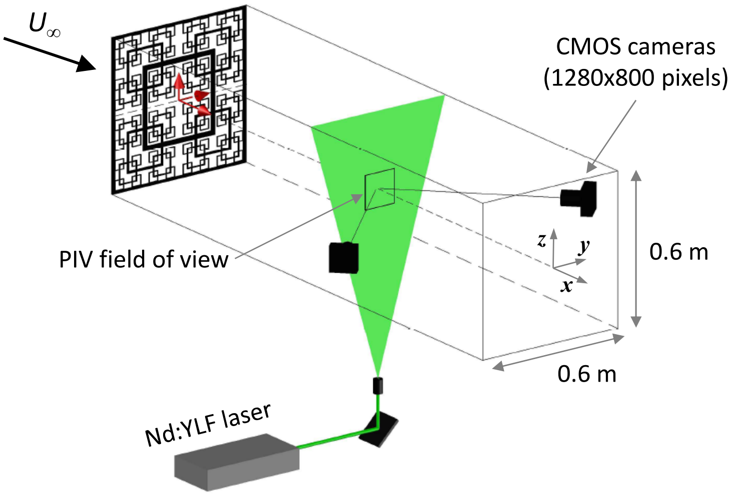

FIGURE 1. Schematic of the water tunnel and PIV setup.

decay regions) and one in the decay region. The measurement stations in the decay and production regions were chosen to have very similar values of Re_λ to facilitate comparisons. The study of fluctuating velocity gradient statistics requires the measurement of the full velocity gradient tensor which, experimentally, has never been done before for turbulence generated by space-filling fractal square grids.

The experimental technique used is cinematographic stereoscopic Particle Image Velocimetry (PIV) and more details of the experimental setup can be found is section 2. The full velocity gradient is determined using Taylor's hypothesis and its validity to the present case is analysed in section 3. Velocity gradient statistics and their spatial development are presented in section 4. Section 5 reports on instantaneous results with reconstructed volumes of enstrophy and strain together with spatial developments of second order structure functions. We conclude in section 6.

2. Experimental details

2.1. *Experimental facility and grid geometry details*

Experiments are carried out in a recirculating water tunnel whose schematic is shown in figure 1. The test section has a cross sectional area of 0.6×0.6 m^2 and it is 9 m long. Transparent perspex sheets are installed as a roof to prevent any gravitational waves to interfere with the flow. The free-stream turbulence intensity is 2.8% for the streamwise fluctuating velocity u and 4.4% for the spanwise fluctuating velocity v. For more details on the experimental facility see Gomes-Fernandes *et al.* (2012).

In the present work, the space-filling fractal square grid SFG17 is used. See figure 2 for a schematic. It has four "fractal iterations" ($N = 4$), a thickness ratio (t_r) of 17 (t_r is the ratio between the lateral thickness of the thickest bar t_0 and of the thinnest bar t_{min}) and a blockage ratio of 25%. L_0 is the distance between the thickest bars and the ratio between the lengths of two consecutive iterations $R_L = L_{i+1}/L_i$ (i from 0 to $N-1$) is 1/2. Defined in a similar way, the ratio between the thickness of two consecutive

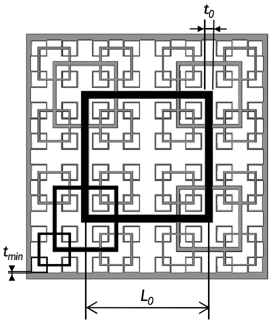

FIGURE 2. Schematic of the SFG17 after Gomes-Fernandes *et al.* (2012). The $N = 4$ "fractal iterations" are highlighted in black and further details on the geometrical parameters are found in table 1.

Grid	N	t_r	t_0 (mm)	t_{min} (mm)	L_0 (mm)	σ (%)
SFG17	4	17	23.5	1.4	303.3	25

TABLE 1. Space-filling fractal square grid SFG17 geometric details.

Case	$U_\infty (ms^{-1})$	Re_{t_0}	Re_{L_0}
A	0.48	11200	144900
C	0.69	16000	208300

TABLE 2. Experimental conditions: free-stream velocities and global Reynolds numbers. Re_{t_0} and Re_{L_0} are the Reynolds numbers based on the thickness t_0 and on the distance L_0 between the thickest bars, respectively (see figure 2): $Re_{t_0} = U_\infty t_0/\nu$ and $Re_{L_0} = U_\infty L_0/\nu$

iterations is $R_t = t_{i+1}/t_i$ is $t_r^{1/(N-1)}$. The grid thickness (or chord) in the streamwise direction is 5 mm. Full geometrical details are found in table 1.

The inlet velocity U_∞ was set to two different values: 0.48 and 0.69 ms^{-1}, case A and C, respectively, of Gomes-Fernandes *et al.* (2012). The results presented in this paper are related to case A unless stated otherwise. Table 2 shows a summary of the inlet velocities and global Reynolds numbers for the present study. The global Reynolds number is set by inlet conditions and does not depend on space and time.

2.2. *Measurement locations*

Figure 3 shows the centreline streamwise evolution of the turbulence intensity of the streamwise velocity fluctuation (u'/U_∞) generated by space-filling fractal square grids from two different experiments (Mazellier & Vassilicos 2010; Gomes-Fernandes *et al.* 2012). The streamwise distance x is normalized by $x_*^{peak} \propto L_0^2/(\alpha C_d t_0)$ (where α is a parameter that takes into account the incoming free-stream turbulence and C_d is the drag coefficient of the thickest bar if assumed of infinite length) which is an estimator of the turbulence intensity peak location and an improvement on the wake interaction length scale introduced by Mazellier & Vassilicos (2010). Turbulence intensity is scaled by $\beta^{-1}(C_d t_0/x_*^{peak})^{1/2}$ where β is another parameter that takes into account the incoming free-stream turbulence. More details on these scalings can be found in Gomes-Fernandes *et al.* (2012).

Measurements of the three velocity components (see next subsection) are made at the

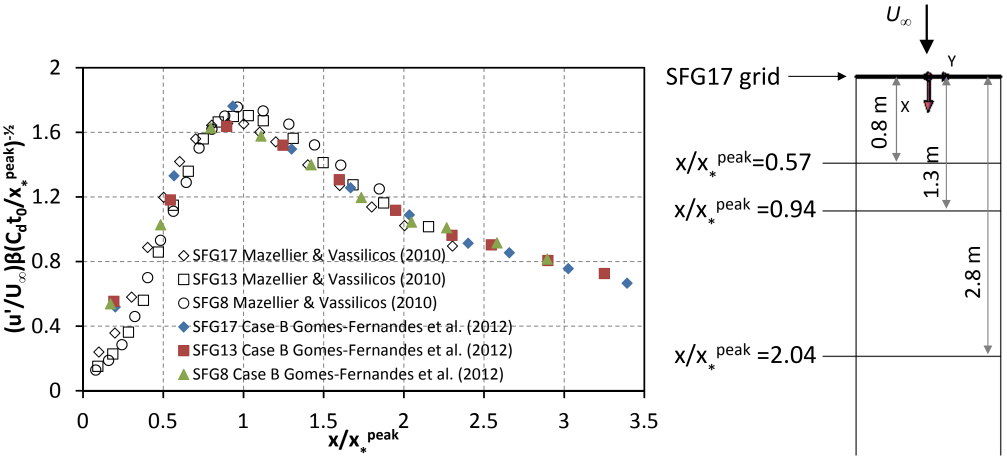

FIGURE 3. Streamwise evolution of the centreline turbulence intensity generated by space-filling square fractal grids after Gomes-Fernandes *et al.* (2012, pp. 325) and a plan view of the measurement locations for the present study.

Station	λ (m)	L (m)
$x/x_*^{peak} = 0.57$	5.8×10^{-3}	52×10^{-3}
$x/x_*^{peak} = 0.94$	6.6×10^{-3}	71×10^{-3}
$x/x_*^{peak} = 2.04$	7.5×10^{-3}	77×10^{-3}

TABLE 3. Taylor (λ) and integral (L) length scales for the measured stations. The integral length scale is computed with data from the study of Gomes-Fernandes *et al.* (2012).

three different streamwise locations shown in figure 3. Locations $x/x_*^{peak} = 0.57$, 0.94 and 2.04 correspond to the production, peak and decay regions, respectively, of the turbulence intensity. Our decay region station is in the non-equilibrium decay region where $C_\epsilon \sim Re_I/Re_\lambda$ (see Valente & Vassilicos 2012; Gomes-Fernandes *et al.* 2012). In the yz plane, the measurements are made in a rectangular field of view centred at the centreline of the tunnel (see figure 1) with approximate dimensions 41 × 22 mm in all three stations. These dimensions correspond to $7.2\lambda \times 3.8\lambda \approx 0.8L \times 0.43L$, $6.3\lambda \times 3.4\lambda \approx 0.59L \times 0.31L$ and $6\lambda \times 3\lambda \approx 0.54L \times 0.29L$ in the y and z directions at stations x/x_*^{peak}=0.57, 0.94 and 2.04, respectively, in terms of the Taylor microscale λ and the integral length scale L of the streamwise velocity along the streamwise distance (see Gomes-Fernandes *et al.* (2012) for the computation of the integral length scale and table 3 for the values of the Taylor and integral length scales at our measurement stations).

2.3. *Experimental technique*

We follow the same procedure as Ganapathisubramani *et al.* (2007), van Doorne & Westerweel (2007), Steinberg *et al.* (2008), Dennis & Nickels (2011) and Gamba *et al.* (2013) and measure the velocity field with a cinematographic stereoscopic Particle Image Velocimetry (PIV) technique. In this particular PIV setup the laser light sheet is perpendicular to the mean flow direction. Figure 1 shows the PIV system which consists of a Nd:YLF laser (Litron LDY304 with 30 mJ/pulse at 1kHz) with an output wavelength of 527 nm and a pair of CMOS cameras (Phantom v210).

The laser light sheet is obtained by bending the beam 90° with a mirror, passing it

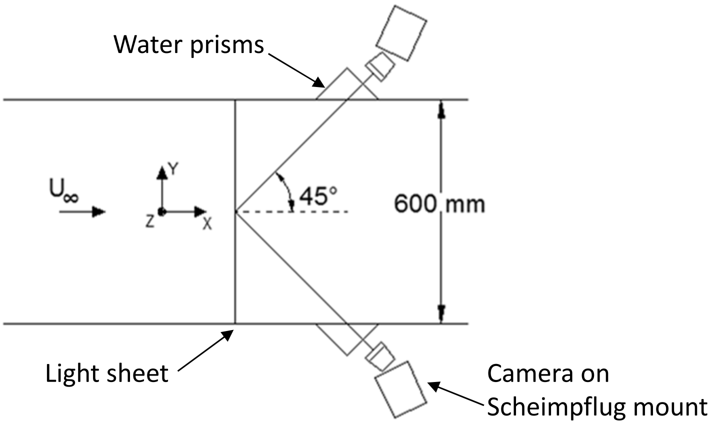

FIGURE 4. PIV setup schematic. Plan view.

through a spherical lens to converge the beam into a minimum thickness of 1.2 mm (measured width between the halves of the maximum power) and through a cylindrical lens to create the light sheet seen in figure 1.

The cameras are operated at a resolution of 1280 x 800 pixels ($20\mu m$ of pixel size) and are synchronized with the laser at a frequency of 2.2 kHz. They are arranged in a 45° degree angle in relation to the grid centreline and the focus is maintained throughout the image using Scheimpflug mounts (see figure 4). Both cameras were fitted with a Nikon 200 mm lens with a f# of 22 to improve focus. The acquisition time per run is 2.7 seconds.

To alleviate the aberrations due to the difference in the refraction index of glass/perspex and water, two water prisms were placed against the side windows (see figure 4) after Prasad & Jensen (1995). The perspective distortion and other aberrations introduced by the water/glass interface were corrected using a calibration target with a fixed grid that was displaced in the x direction with increments of 0.5 mm. A third-order polynomial function after Soloff *et al.* (1997) is fitted to map the vectors from image to object plane.

The flow is seeded with silver coated silica with a nominal size of 2 μm and a specific gravity of around 2.5. The response time (τ_P) of the seeding particles is estimated to be 0.3 μs. The Stokes number $St = \tau_P/\tau_F$ is estimated using the Kolmogorov time scale $\tau_\eta = \sqrt{\nu/\epsilon}$ (where ν is the water kinematic viscosity and ϵ is the turbulent kinetic energy dissipation) as the characteristic time scale (τ_F). For the particles to faithfully follow the turbulent flow this number has to be substantially less than one. In our case $St = 5.4 \times 10^{-6}$.

The images were acquired in single frame mode. Frame 1 was correlated with frame 2 to get the first velocity field, frames 3 and 4 to get the second one and so forth. The final interrogation window size was 32×32 pixels with 75% overlap. On average, more than 8 particles are interrogated per window. The number of spurious vectors was less than 1%. Table 4 shows the experimental resolution at each station (the resolution is stated in terms of the Kolmogorov length scale).

Figure 5 shows two consecutive velocity fields in the yz plane (both directions y and

Station	x direction ($U/2200$)	yz plane (interrogation window size)	lightsheet thickness (1.2mm)
$x/x_*^{peak} = 0.57$	1.4η	4.3η	4.5η
$x/x_*^{peak} = 0.94$	1.4η	4.8η	5.2η
$x/x_*^{peak} = 2.04$	0.9η	3.4η	3.8η

TABLE 4. Spatial resolution in terms of the Kolmogorov length scale. In the x direction the resolution is computed using the local mean flow velocity U and the frequency between laser pulses, 2200 Hz. In the yz plane the resolution is related to the interrogation window size. Finally, the light sheet thickness is also shown in terms of the Kolmogorov length scale.

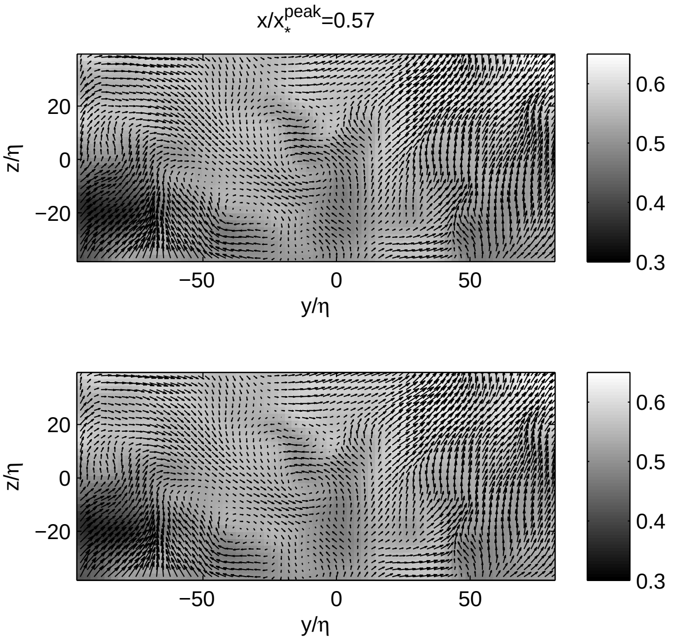

FIGURE 5. A sequence of two consecutive instantaneous vector fields at $x/x_*^{peak} = 0.57$. The grey scale background shows the velocity (ms^{-1}) in the x direction.

z are normalised by the Kolmogorov scale η). The grey scale background shows the full velocity, $\tilde{u}$, in the x direction (where $\tilde{u} = U + u$, the sum of the mean and fluctuating velocity components) and the vector arrows show the $\tilde{v} \approx v$ and $\tilde{w} \approx w$ components in the y and z directions, respectively, since the mean velocity components V and W are negligible (effectively they amount to less than 2% of U). The two vector fields are similar suggesting that, for our PIV temporal resolution, Taylor's hypothesis can be applied to reconstruct a quasi-instantaneous velocity volume with the cinematographic PIV data. Data in the other two stations show similar behaviour and are not shown here for brevity.

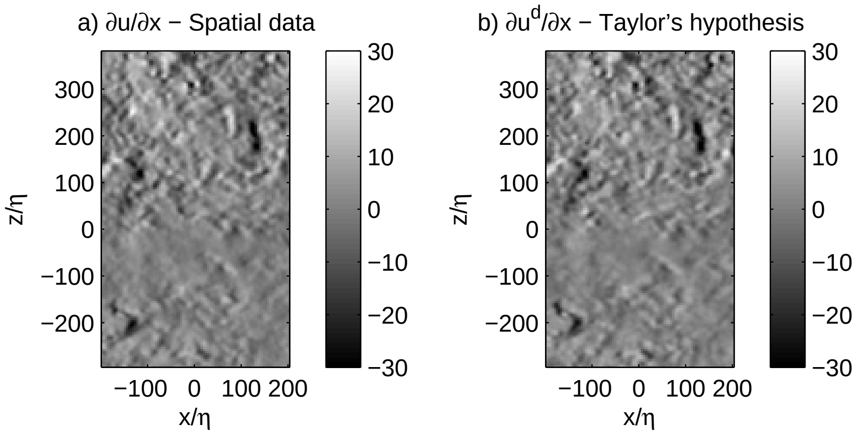

FIGURE 6. A sample of velocity gradients computed by spatial data, $\partial u/\partial x$, and by using Taylor's hypothesis, $\partial u^d/\partial x$, at $x/x_*^{peak} = 0.57$.

3. Assessment of Taylor's hypothesis

The experimental setup in the present study requires that Taylor's hypothesis is valid in order to compute the velocity fluctuation gradients in the streamwise direction. This section is dedicated to the validation of this hypothesis.

Velocity gradients are sensitive to noise present in the data. To reduce the effect of noise, a 3D Gaussian filter was applied. The 3D kernel is based on a Gaussian function with a Full Width at Half Maximum (FWHM) equal to the experimental resolution in the yz plane (see table 4) at each measurement station.

The validity of Taylor's hypothesis is assessed by means of a separate experiment with only one high speed camera measuring a two component (2C) velocity field in the xz plane. The 2C PIV setup has different parameters from the stereo experiment, namely a larger field of view (180 × 100 mm in the z and x directions respectively) and a shorter acquisition rate (500 Hz) in order for the time resolution to match the new spatial resolution. The final interrogation window was 16 × 16 pixels with 50% overlap which yielded a resolution of around 8.3η (size of the interrogation window). A 3D Gaussian filter was also applied here with a FWHM equal to the resolution. Using Ganapathisubramani *et al.* (2007) notation, the velocity gradient field is computed using Taylor's hypothesis by

$$\frac{\partial u^d(x,z)}{\partial x} = \frac{-1}{U(x,z)} \frac{\partial u(x,z)}{\partial t} \tag{3.1}$$

$$\frac{\partial w^d(x,z)}{\partial x} = \frac{-1}{U(x,z)} \frac{\partial w(x,z)}{\partial t} \tag{3.2}$$

where $U(x,z)$ is, again, the average streamwise velocity where the average is computed over time.

Figure 6 shows a sample of an instantaneous velocity gradient field computed by spatial data and the derived gradient (superscript d) from equation 3.1 where the local position $x/\eta = 0$ corresponds to the global position $x/x_*^{peak} = 0.57$ and $z/\eta = 0$ corresponds to the centreline (the other two station show similar results and are not shown here for brevity).

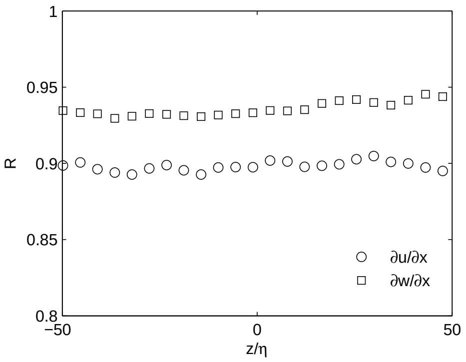

FIGURE 7. Correlation coefficients between $\partial u/\partial x$ and $\partial u^d/\partial x$ and between $\partial w/\partial x$ and $\partial w^d/\partial x$ at $x/x_*^{peak} = 0.57$.

The two plots show similarities, especially between the high magnitude gradients. The same is seen for the gradients computed from equation 3.2 and not presented here for brevity. In order to quantify these similarities the correlation coefficients between $\partial u/\partial x$ and $\partial u^d/\partial x$ and between $\partial w/\partial x$ and $\partial w^d/\partial x$ are presented in figure 7 at $x/x_*^{peak} = 0.57$. The correlation coefficient is averaged over time for the points along the z direction located at $x/x_*^{peak} = 0.57$. In this figure $z/\eta = 0$ corresponds to the centreline of the fractal grid and the $z/\eta = \pm 50$ corresponds to a representative range captured by the stereo PIV experiment. The correlation coefficients appear to be constant in this range with values around 0.9 for $\partial u/\partial x$ and 0.94 for $\partial w/\partial x$, consistent with the results of Ganapathisubramani *et al.* (2007).

4. Statistical results

Westerweel (1993) showed that the vorticity could be computed to within 10 to 20% accuracy provided that the velocity measurement uncertainty is between 1 to 2% accurate. Ganapathisubramani *et al.* (2007) calculated a relative uncertainty close to 15% of the velocity gradient rms by applying Raffel's error propagation analysis (Raffel 2007) to a turbulent jet with the same PIV measurement setup as the present study. In the present case the relative error in our velocity fluctuations is estimated on the basis of a sub-pixel interpolation rms uncertainty of 0.1 pixels. The pixel displacement is on average 6 pixels in our setup which gives a relative uncertainty in the velocity measurements of the order of 1.7%, within the aforementioned range.

To improve the accuracy of the statistics presented in this paper, the results will be conditioned on points where there is a small value of the divergence error. Buxton *et al.* (2011) showed that this procedure improves the similarity to results where the divergence-free criterion is fully met such as in Direct Numerical Simulations (DNS). Lüthi *et al.* (2005) and Gulitski *et al.* (2007) also used this procedure without, however, showing how it improves statistics as extensively as Buxton *et al.* (2011). A detailed analysis of the measurement accuracy for the present study in terms of the divergence error is presented in the Appendix.

The criterion for choosing which level of divergence error is acceptable is related to the statistical convergence of the results. For each station the full velocity gradient field is computed in a volume of 150 × 80 × 2726 points in the y, z and x directions (where the x direction is time information converted to space), respectively, totalling 32.712.000

points (same for all three stations). In the present case, the statistics for each station will be conditioned to points where the absolute value of the first invariant of the velocity gradient tensor characteristic equation, $|P| = |-(\partial u/\partial x + \partial v/\partial y + \partial w/\partial z)|$, is less than $0.02(\nu/\eta^2)$ (which is equal to $2\times 10^{-6}(\nu/L^2)$ and to $2\times 10^{-3}(u'/L)$). This condition results in around three million points at each station. We define the correlation coefficient between $\partial u/\partial x$ and $-(\partial v/\partial y + \partial w/\partial z)$ as C_T. These conditional statistics set the correlation coefficient, C_T, to values above 0.99 for all three stations. We also condition $|P|$ to be less than $0.08(\nu/\eta^2)$ to statistically converge lower probability contours. The C_T takes values around 0.95 in this case. Whenever conditional probabilities are performed, there is an indication of the value which P is conditioned on.

The second (Q) and third (R) invariants of the characteristic equation of the velocity gradient tensor are defined, for incompressible flows, as

$$Q = \frac{1}{4}(\omega_i\omega_i - 2s_{ij}s_{ji}) \tag{4.1}$$

$$R = -\frac{1}{3}(s_{ij}s_{jk}s_{ki} + \frac{3}{4}\omega_i s_{ij}\omega_j) \tag{4.2}$$

where s_{ij} and ω_i are the strain rate and vorticity, respectively, of the velocity fluctuations. It is useful to decompose the above invariants into contributions from the symmetric and skew-symmetric parts of the velocity gradient tensor. The second invariant is decomposed as $Q = Q_s + Q_\omega$ where

$$Q_s = -\frac{1}{2}s_{ij}s_{ji} \tag{4.3}$$

$$Q_\omega = \frac{1}{4}\omega_i\omega_i\ . \tag{4.4}$$

The third invariant is decomposed as $R = R_s + R_\omega$ where

$$R_s = -\frac{1}{3}s_{ij}s_{jk}s_{ki} \tag{4.5}$$

$$R_\omega = -\frac{1}{4}\omega_i s_{ij}\omega_j\ . \tag{4.6}$$

For homogeneous flows it can be proved that $\langle Q\rangle = 0$ and $\langle R\rangle = 0$ given that $\langle Q\rangle$ and $\langle R\rangle$ can be written as a divergence of an average (we use $\langle ...\rangle$ to denote spatial averaging in the yz plane together with a temporal average in the x direction). It was shown by Mazellier & Vassilicos (2010) that the flow is highly inhomogeneous in terms of one-point mean flow and turbulence intensity profiles upstream of the turbulence intensity peak. For $x/x_*^{peak} > 1$, Seoud & Vassilicos (2007), Mazellier & Vassilicos (2010) and Valente & Vassilicos (2011) showed that the flow is approximately homogeneous in the mean and turbulence profiles (i.e. they vary by up to 10 and 15%, respectively, over a transverse distance about the centreline equal to L_0) but not in third order statistics such as pressure and turbulence transport (at least for the distances studied). We find that $\langle R_\omega\rangle < 0$ and $\langle R_s\rangle > 0$ in all our three stations and that $-0.91\,\langle Q_s\rangle < \langle Q_\omega\rangle < -0.89\,\langle Q_s\rangle$ and $0.89\,\langle R_s\rangle < -\langle R_\omega\rangle < 0.92\,\langle R_s\rangle$ (figure 8). Hence $\langle Q\rangle$ and $\langle R\rangle$ have the same sign as and are an order of magnitude smaller than $\langle Q_s\rangle$ and $\langle R_s\rangle$ respectively. In this sense, $\langle Q\rangle$ and $\langle R\rangle$ are close to zero but not quite and the turbulence is therefore locally homogeneous, even though it is not homogeneous in the sense mentioned a few lines above in this

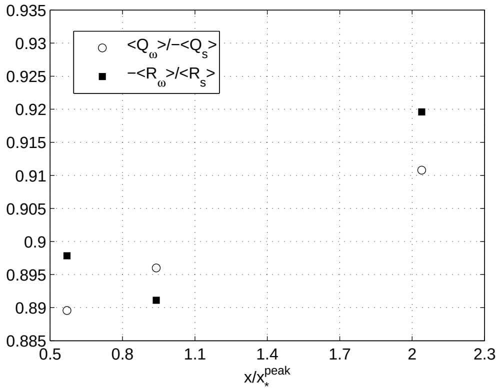

FIGURE 8. Spatial evolution of the ratios $\langle Q_\omega \rangle / -\langle Q_s \rangle$ and $-\langle R_\omega \rangle / \langle R_s \rangle$.

paragraph. It is this local homogeneity which matters here as described in the next few paragraphs.

Considering the mean shear contribution, the equations for the mean enstrophy, $\langle \omega^2 \rangle$ (Tennekes & Lumley 1972), and strain, $\langle s_{ij}s_{ij} \rangle$ (Yanitskii 1982), of the turbulent fluctuations can be written as:

$$\frac{1}{2}U\frac{\partial \langle \omega^2 \rangle}{\partial x} = -\frac{1}{2}\frac{\partial}{\partial x}\langle u\omega_i\omega_i \rangle + \langle \omega_i s_{ij}\omega_j \rangle + \langle \omega_1^2 \rangle S_{11} + \nu \langle \omega_i \nabla^2 \omega_i \rangle \tag{4.7}$$

and

$$\begin{aligned} \frac{1}{2}U\frac{\partial \langle s_{ij}s_{ij} \rangle}{\partial x} = &- \langle us_{11} \rangle \frac{\partial S_{11}}{\partial x} - \frac{1}{2}\frac{\partial}{\partial x}\langle us_{ij}s_{ij} \rangle - 2\langle s_{i1}s_{i1} \rangle S_{11} \\ &- \langle s_{ij}s_{jk}s_{ki} \rangle - \frac{1}{4}\langle \omega_i s_{ij}\omega_j \rangle - \left\langle s_{ij}\frac{\partial^2 p}{\partial x_i \partial x_j} \right\rangle + \nu \langle s_{ij}\nabla^2 s_{ij} \rangle \end{aligned} \tag{4.8}$$

taking into account that the average $\langle ... \rangle$ is performed in the yz plane and time and, therefore, the derivatives in those directions cancel out here. S_{ij} are the components of the mean flow's strain and Ω_i, which is the "ith" component of the mean flow vorticity, is approximately zero given that the fields of view are taken around the centreline ($i = 1, 2, 3$ correspond to x, y, z orientations respectively). Table 5 gives a summary of the main quantities related to the velocity gradient tensor presented throughout the present study.

In this study we only consider the derivatives of the velocity fluctuations. The derivatives of the mean flow are negligible by comparison within our field of view. Figures 9a and 9b show the mean velocity profiles (in this case obtained by averaging only over time) of the streamwise component in the z and y directions, respectively. The maximum value of the mean velocity gradient is found to be in figure 9a and specifically at $z/\eta \approx 50$. The value of $\partial U/\partial z$ at this position is close to that of $\partial U/\partial x$ at the centreline. In the following paragraph we show that the terms related to $\partial U/\partial x$ in equations 4.7 and 4.8 are negligible and, therefore, we expect the same in relation to the terms containing $\partial U/\partial z$ for the size of the field of view considered here.

Indeed the contributions to strain production associated with mean velocity gradients such as $\langle s_{i1}s_{i1} \rangle S_{11}$ and $\langle us_{11} \rangle \partial S_{11}/\partial x$ (see equation 4.8) amount to 0.027 and 4.5×10^{-7}, respectively, of $\langle s_{ij}s_{jk}s_{ki} \rangle$ and a similar trend is verified for the enstrophy production term $\langle \omega_1^2 \rangle S_{11}$ (see equation 4.7) which is 0.038 of $\langle \omega_i s_{ij}\omega_j \rangle$. All of the aforementioned

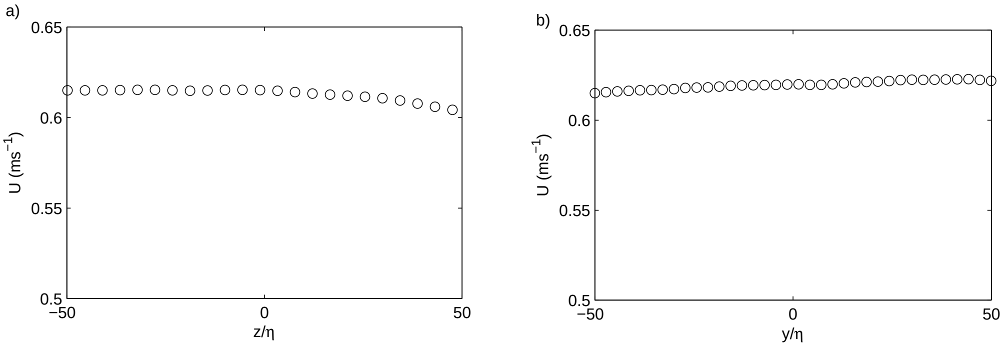

FIGURE 9. Mean velocity profiles of the streamwise velocity component, U, at $x/x_*^{peak} = 0.57$ in the z and y directions. V and W, the mean velocities in the y and z directions, respectively, amount for a maximum of 2% of U and therefore are considered negligible. Mean velocity components are obtained by averaging only over time in this figure.

Quantity	Description	Equation
P, Q and R	first, second and third invariants of the velocity gradient tensor	4.1 and 4.2
Q_s and R_s	second and third invariants of the strain-rate tensor	4.3 and 4.5
Q_ω and R_ω	second and third invariants of the rotation-rate tensor	4.4 and 4.6
λ_i and e_i	eigenvalues and eigenvectors, respectively, of the strain-rate tensor	N/A
$s_{ij}s_{ji}$	strain level	N/A
$\omega_i\omega_i$	enstrophy level	N/A
$-s_{ij}s_{jk}s_{ki}$	strain self-amplification	4.8
$\omega_i s_{ij}\omega_j$	enstrophy production	4.7
$\omega_i^2\lambda_i cos^2(\omega, e_i)$	i^{th} eingenvalue and eigenvector contribution to enstrophy production	4.12

TABLE 5. Summary of velocity gradient tensor quantities.

ratios are given for the location $x/x_*^{peak} = 0.57$ where we found them to be the largest of all three measurement stations.

4.1. *Strain rate and enstrophy production*

Figure 10 shows the spatial evolution of $\langle s_{ij}s_{ji}\rangle$, $-\langle s_{ij}s_{jk}s_{ki}\rangle$ and $\langle \omega_i s_{ij}\omega_j\rangle$ normalised by the inverse time scale U_∞/x_*^{peak} where U_∞ is the freestream velocity (table 2) and x_*^{peak}=1.36m is an estimator of the turbulence peak location in the streamwise direction along the centreline according to Gomes-Fernandes *et al.* (2012). The fluctuating strain

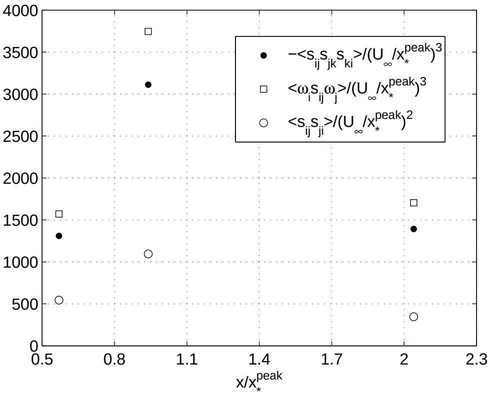

FIGURE 10. Spatial evolution of $-\langle s_{ij}s_{jk}s_{ki}\rangle/(U_\infty/x_*^{peak})^3$, $\langle \omega_i s_{ij}\omega_j\rangle/(U_\infty/x_*^{peak})^3$ and $\langle s_{ij}s_{ji}\rangle/(U_\infty/x_*^{peak})^2$. U_∞ is the freestream velocity (table 2) and x_*^{peak}=1.36m is an estimator of the turbulence peak location in the streamwise direction along the centreline according to Gomes-Fernandes *et al.* (2012).

x/x_*^{peak}	0.57	0.94	2.04
$\langle \omega_i s_{ij}\omega_j\rangle / \langle s_{ij}s_{ji}\rangle^{3/2}$	0.123	0.103	0.263
$-\langle s_{ij}s_{jk}s_{ki}\rangle / \langle s_{ij}s_{ji}\rangle^{3/2}$	0.103	0.086	0.215

TABLE 6. Ratios between enstrophy production $\langle \omega_i s_{ij}\omega_j\rangle$ and the strain self-amplification $-\langle s_{ij}s_{jk}s_{ki}\rangle$ terms in relation to the strain level at each of our measured stations.

level increases substantially from $x/x_*^{peak} = 0.57$ to 0.94, in fact doubles from the station at the production region to the peak and then decreases in the decay region, as seen at x/x_*^{peak}=2.04.

The enstrophy production $\langle \omega_i s_{ij}\omega_j\rangle$ (equation 4.7) and the strain self-amplification $-\langle s_{ij}s_{jk}s_{ki}\rangle$ (equation 4.8) terms (both positive) also increase from $x/x_*^{peak} = 0.57$ to 0.94 and decay afterwards as seen at $x/x_*^{peak} = 2.04$. Table 6 shows these quantities normalised by $\langle s_{ij}s_{ji}\rangle^{3/2}$; $\langle \omega_i s_{ij}\omega_j\rangle$ and $-\langle s_{ij}s_{jk}s_{ki}\rangle$ remain roughly about the same proportion of $\langle s_{ij}s_{ji}\rangle^{3/2}$ at x/x_*^{peak}=0.57 and 0.94. Then, these quantities decrease in the decay region (figure 10) but grow (in fact more than double) in proportion to the decaying $\langle s_{ij}s_{ji}\rangle^{3/2}$. Hence, perhaps surprisingly, their decay is slower than that of $\langle s_{ij}s_{ji}\rangle^{3/2}$, and it is natural to ask why.

More detail on what happens and an answer to this question can be obtained on the basis of the following two relations:

$$\langle s_{ij}s_{jk}s_{ki}\rangle = \left\langle \lambda_1^3\right\rangle + \left\langle \lambda_2^3\right\rangle + \left\langle \lambda_3^3\right\rangle \tag{4.9}$$

and

$$\langle \omega_i s_{ij}\omega_j\rangle = \left\langle \omega_1^2\lambda_1 cos^2(\omega,e_1)\right\rangle + \left\langle \omega_2^2\lambda_2 cos^2(\omega,e_2)\right\rangle + \left\langle \omega_3^2\lambda_3 cos^2(\omega,e_3)\right\rangle \tag{4.10}$$

which follow from:

$$s_{ij}s_{jk}s_{ki} = \lambda_1^3 + \lambda_2^3 + \lambda_3^3 \tag{4.11}$$

x/x_*^{peak}	0.57	0.94	2.04	Field experiment
$\left\langle\lambda_1^3\right\rangle/(U_\infty/x_*^{peak})^3$	5897	14267	2181	–
$\left\langle\lambda_2^3\right\rangle/(U_\infty/x_*^{peak})^3$	64	154	77	–
$\left\langle\lambda_3^3\right\rangle/(U_\infty/x_*^{peak})^3$	-7260	-17561	-3645	–
$\left\langle\lambda_1^3\right\rangle/\left\langle s_{ij}s_{ji}\right\rangle^{3/2}$	0.46	0.39	0.34	–
$\left\langle\lambda_2^3\right\rangle/\left\langle s_{ij}s_{ji}\right\rangle^{3/2}$	0.005	0.004	0.012	–
$\left\langle\lambda_3^3\right\rangle/\left\langle s_{ij}s_{ji}\right\rangle^{3/2}$	-0.57	-0.48	-0.56	–
$\left\langle\lambda_1^3\right\rangle/-\left\langle s_{ij}s_{jk}s_{ki}\right\rangle$	4.54	4.54	1.57	1.62
$\left\langle\lambda_2^3\right\rangle/-\left\langle s_{ij}s_{jk}s_{ki}\right\rangle$	0.05	0.05	0.06	0.05
$\left\langle\lambda_3^3\right\rangle/-\left\langle s_{ij}s_{jk}s_{ki}\right\rangle$	-5.59	-5.59	-2.63	-2.67

TABLE 7. Ratios between $\left\langle\lambda_i^3\right\rangle$ (for $i = 1$ to 3) and $(U_\infty/x_*^{peak})^3$, $\left\langle s_{ij}s_{ji}\right\rangle^{3/2}$ and $-\left\langle s_{ij}s_{jk}s_{ki}\right\rangle$. The values of the field experiment in the atmospheric surface layer case were taken from Kholmyansky *et al.* (2001).

and

$$\omega_i s_{ij}\omega_j = \omega_1^2\lambda_1 cos^2(\omega, e_1) + \omega_2^2\lambda_2 cos^2(\omega, e_2) + \omega_3^2\lambda_3 cos^2(\omega, e_3) \tag{4.12}$$

where e_i and λ_i (for i=1 to 3) are the eigenvectors and eigenvalues, respectively, of the fluctuating strain rate tensor. Ordering λ_i as follows, $\lambda_1 > \lambda_2 > \lambda_3$, and knowing that for incompressible flows $\lambda_1+\lambda_2+\lambda_3 = 0$, then the first eigenvector (e_1) is associated with the extensive eigenvalue ($\lambda_1 > 0$), the third eigenvector (e_3) with the compressive eigenvalue ($\lambda_3 < 0$) and the second, intermediate, eigenvector (e_2) can be either compressive or extensive.

Table 7 shows $\left\langle\lambda_i^3\right\rangle$ (for $i = 1$ to 3) normalised by $(U_\infty/x_*^{peak})^3$, $\left\langle s_{ij}s_{ji}\right\rangle^{3/2}$ and $-\left\langle s_{ij}s_{jk}s_{ki}\right\rangle$. $\left\langle\lambda_1^3\right\rangle$ and $-\left\langle\lambda_3^3\right\rangle$ normalised by $(U_\infty/x_*^{peak})^3$ increase substantially from $x/x_*^{peak} = 0.57$ to 0.94 but remain about the same proportion of $-\left\langle s_{ij}s_{jk}s_{ki}\right\rangle$ in these two locations. Their increase is therefore simply a reflection of the increase of $-\left\langle s_{ij}s_{jk}s_{ki}\right\rangle$. They then decrease in x/x_*^{peak}=2.04 but their proportion of $-\left\langle s_{ij}s_{jk}s_{ki}\right\rangle$ also decreases there.

Comparing this behaviour with the observation that $-\left\langle s_{ij}s_{jk}s_{ki}\right\rangle$ decreases slower than $\left\langle s_{ij}s_{ji}\right\rangle^{3/2}$ in this region, we see that $\left\langle\lambda_3^3\right\rangle/\left\langle s_{ij}s_{ji}\right\rangle^{3/2}$ varies little across the three stations and $\left\langle\lambda_1^3\right\rangle/\left\langle s_{ij}s_{ji}\right\rangle^{3/2}$ and $\left\langle\lambda_2^3\right\rangle/\left\langle s_{ij}s_{ji}\right\rangle^{3/2}$ vary more substantially. Even though $\left\langle\lambda_2^3\right\rangle/\left\langle s_{ij}s_{ji}\right\rangle^{3/2}$ at x/x_*^{peak}=2.04 is three times its value at x/x_*^{peak}=0.94, it still has a negligible effect on the overall $-\left\langle s_{ij}s_{jk}s_{ki}\right\rangle/\left\langle s_{ij}s_{ji}\right\rangle^{3/2}$. On the other hand, $\left\langle\lambda_1^3\right\rangle/\left\langle s_{ij}s_{ji}\right\rangle^{3/2}$ decreases considerably which contributes to an increase in the magnitude of $-\left\langle s_{ij}s_{jk}s_{ki}\right\rangle/\left\langle s_{ij}s_{ji}\right\rangle^{3/2}$. Therefore the fact that $-\left\langle s_{ij}s_{jk}s_{ki}\right\rangle$ decays slower than $\left\langle s_{ij}s_{ji}\right\rangle^{3/2}$ (see table 6) is due to the asymmetric evolution of $\left\langle\lambda_1^3\right\rangle/\left\langle s_{ij}s_{ji}\right\rangle^{3/2}$ in relation to $\left\langle\lambda_3^3\right\rangle/\left\langle s_{ij}s_{ji}\right\rangle^{3/2}$, specifically the fact that the positive values of $\left\langle\lambda_1^3\right\rangle/\left\langle s_{ij}s_{ji}\right\rangle^{3/2}$ decrease while the negative values of $\left\langle\lambda_3^3\right\rangle/\left\langle s_{ij}s_{ji}\right\rangle^{3/2}$ are about the same in our production and decay stations.

The reason why $\left\langle\omega_i s_{ij}\omega_j\right\rangle$ decays slower than $\left\langle s_{ij}s_{ji}\right\rangle^{3/2}$ is based on a different phenomenon. Table 8 shows the contributions from each eigenvector to the total mean

x/x_*^{peak}	0.57	0.94	2.04	Grid	Field experiment
$\left\langle \omega_1^2 \lambda_1 cos^2(\omega, e_1) \right\rangle / (U_\infty / x_*^{peak})^3$	5023	13674	2693	–	–
$\left\langle \omega_2^2 \lambda_2 cos^2(\omega, e_2) \right\rangle / (U_\infty / x_*^{peak})^3$	660	1237	665	–	–
$\left\langle \omega_3^2 \lambda_3 cos^2(\omega, e_3) \right\rangle / (U_\infty / x_*^{peak})^3$	-4114	-11165	-1637	–	–
$\left\langle \omega_1^2 \lambda_1 cos^2(\omega, e_1) \right\rangle / \left\langle s_{ij} s_{ji} \right\rangle^{3/2}$	0.39	0.38	0.42	–	–
$\left\langle \omega_2^2 \lambda_2 cos^2(\omega, e_2) \right\rangle / \left\langle s_{ij} s_{ji} \right\rangle^{3/2}$	0.052	0.034	0.103	–	–
$\left\langle \omega_3^2 \lambda_3 cos^2(\omega, e_3) \right\rangle / \left\langle s_{ij} s_{ji} \right\rangle^{3/2}$	-0.32	-0.31	-0.25	–	–
$\left\langle \omega_1^2 \lambda_1 cos^2(\omega, e_1) \right\rangle / \left\langle \omega_i s_{ij} \omega_j \right\rangle$	3.2	3.65	1.58	1.17	1.44
$\left\langle \omega_2^2 \lambda_2 cos^2(\omega, e_2) \right\rangle / \left\langle \omega_i s_{ij} \omega_j \right\rangle$	0.42	0.33	0.39	0.39	0.47
$\left\langle \omega_3^2 \lambda_3 cos^2(\omega, e_3) \right\rangle / \left\langle \omega_i s_{ij} \omega_j \right\rangle$	-2.62	-2.98	-0.96	-0.56	-0.97
Re_λ	271	364	257	75	10^4

TABLE 8. Detailed contribution from the eigenvalues of the strain rate tensor to the enstrophy production rate. The values are normalized with $(U_\infty / x_*^{peak})^3$, $\left\langle s_{ij} s_{ji} \right\rangle^{3/2}$ and $\left\langle \omega_i s_{ij} \omega_j \right\rangle$. The values of the regular grid case were taken from Tsinober (2009) and the field experiment in atmospheric surface layer case from Kholmyansky *et al.* (2001). $Re_\lambda = u' \lambda / \nu$ where u' is the r.m.s. of the streamwise velocity fluctuation, $\lambda = \sqrt{u^2 / (\partial u / \partial x)^2}$ is the Taylor microscale and ν is the kinematic viscosity.

enstrophy production rate $\left\langle \omega_i s_{ij} \omega_j \right\rangle$ and also shows these contributions normalised by $(U_\infty / x_*^{peak})^3$ and $\left\langle s_{ij} s_{ji} \right\rangle^{3/2}$. Two reference cases are added, one from Tsinober (2009) (regular grid turbulence) and one from Kholmyansky *et al.* (2001) (field experiment in atmospheric surface layer) for comparison. Similarly to the behaviour of $\left\langle \lambda_1^3 \right\rangle$ and $- \left\langle \lambda_3^3 \right\rangle$, $\left\langle \omega_1^2 \lambda_1 cos^2(\omega, e_1) \right\rangle$ and $\left\langle \omega_3^2 \lambda_3 cos^2(\omega, e_3) \right\rangle$ increase substantially from the production region to the peak (as seen in $(U_\infty / x_*^{peak})^3$ units) but remain about the same proportion of $\left\langle \omega_i s_{ij} \omega_j \right\rangle$ in these two places. Their increase is therefore simply a reflection of the increase of $\left\langle \omega_i s_{ij} \omega_j \right\rangle$. They then decrease in the decay region but their proportion of $\left\langle \omega_i s_{ij} \omega_j \right\rangle$ also decreases there.

The values of $\left\langle \omega_1^2 \lambda_1 cos^2(\omega, e_1) \right\rangle / \left\langle s_{ij} s_{ji} \right\rangle^{3/2}$ and $\left\langle \omega_3^2 \lambda_3 cos^2(\omega, e_3) \right\rangle / \left\langle s_{ij} s_{ji} \right\rangle^{3/2}$ are, respectively, similar at x/x_*^{peak}=0.57 and 0.94 but change significantly at x/x_*^{peak}=2.04. The same observation can be made for $\left\langle \omega_2^2 \lambda_2 cos^2(\omega, e_2) \right\rangle / \left\langle s_{ij} s_{ji} \right\rangle^{3/2}$ which triples its value form x/x_*^{peak}=0.94 to 2.04. Equation 4.10 shows that the enstrophy production term depends on the eigenvalues but also on the alignment between the eigenvectors and the vorticity vector. The first eigenvalue ($\lambda_1 > 0$) contributes positively to the enstrophy production term and to vortex stretching while the third eigenvalue ($\lambda_3 < 0$) contributes to vortex compression. The behaviour of $\left\langle \lambda_1^3 \right\rangle$ and $\left\langle \lambda_3^3 \right\rangle$ is seen to be an asymmetric evolution from the peak to the decay region where $\left\langle \lambda_1^3 \right\rangle / \left\langle s_{ij} s_{ji} \right\rangle^{3/2}$ takes smaller values and $\left\langle \lambda_3^3 \right\rangle / \left\langle s_{ij} s_{ji} \right\rangle^{3/2}$ remains approximately constant throughout all our stations. If we were to neglect the effect of alignments, then these evolutions of λ_1 and λ_3 would have implied that vortex stretching should decay whilst vortex compression should remain the same and therefore that $\left\langle \omega_i s_{ij} \omega_j \right\rangle / \left\langle s_{ij} s_{ji} \right\rangle^{3/2}$ should decrease in the decay region, which is not the case (see table 6). Therefore the alignments must play a decisive role on the behaviour of $\left\langle \omega_i s_{ij} \omega_j \right\rangle / \left\langle s_{ij} s_{ji} \right\rangle^{3/2}$.

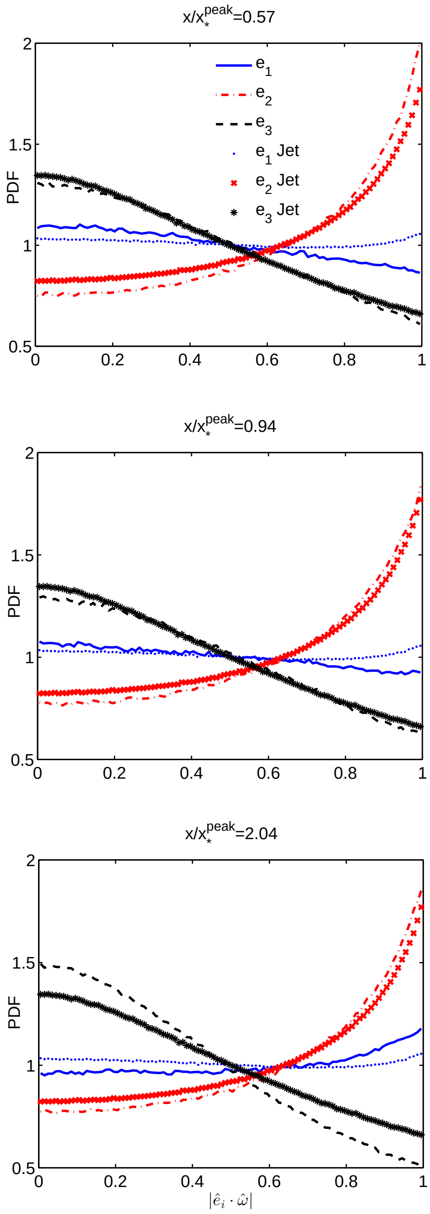

FIGURE 11. Spatial evolution of the alignments of the vorticity vector (ω) with the eigenvectors of the strain rate tensor (e_i for i=1 to 3). Data conditioned to values where $|P| < 0.02(\nu/\eta^2)$. Additional data from Buxton & Ganapathisubramani (2010) for an axisymmetric jet at a fixed streamwise distance of $32D$ (where D is the diameter of the jet nozzle) is presented for comparison.

Figure 11 shows the spatial evolution of the alignments. Far field axisymmetric jet data from Buxton & Ganapathisubramani (2010) at a fixed streamwise distance of $32D$ (where D is the diameter of the jet nozzle) are added for comparison. The second eigenvector e_2 is most likely aligned with vorticity at all stations similar to the jet data. This alignment partly accounts for the significant magnitude of $\left\langle \omega_2^2 \lambda_2 cos^2(\omega, e_2)\right\rangle / \left\langle s_{ij}s_{ji}\right\rangle^{3/2}$ at

x/x_*^{peak}=2.04. The other reason why this term is quite high at this station is the fact that $\left\langle\lambda_2^3\right\rangle/\left\langle s_{ij}s_{ji}\right\rangle^{3/2}$ also increases substantially here (see table 7). The main differences in the alignments, both in terms of spatial development and in comparison to the jet data, are related to the stretching (e_1) and compressing (e_3) eigenvectors. Qualitatively, at x/x_*^{peak}=0.57 vorticity is slightly misaligned with e_1 for the fractal grid turbulence case (Ashurst *et al.* (1987) found a similar behaviour in isotropic and shear flow simulations) whereas it is slightly aligned for the jet case. The spatial evolution of e_1 shows that at the most downstream station it becomes slightly aligned with vorticity which tends to be in qualitative agreement with the jet data. The compressing eigenvector e_3 behaves similarly at x/x_*^{peak}=0.57 and x/x_*^{peak}=0.94 where there is good agreement between the fractal grid turbulence and the jet data. However, at x/x_*^{peak}=2.04 it evolves to be more misaligned in fractal grid turbulence than in the far field of the jet.

The alignment change of the first and third eigenvectors with respect to vorticity from the production and peak stations to the decay station explain why $\left\langle\omega_1^2\lambda_1 cos^2(\omega,e_1)\right\rangle/\left\langle s_{ij}s_{ji}\right\rangle^{3/2}$ increases even though $\left\langle\lambda_1^3\right\rangle/\left\langle s_{ij}s_{ji}\right\rangle^{3/2}$ decreases and why the negative value of $\left\langle\omega_3^2\lambda_3 cos^2(\omega,e_3)\right\rangle/\left\langle s_{ij}s_{ji}\right\rangle^{3/2}$ decreases in magnitude while $\left\langle\lambda_3^3\right\rangle/\left\langle s_{ij}s_{ji}\right\rangle^{3/2}$ remains about constant from peak/production to decay. Therefore, the evolution of the alignments but also the magnitude of $\left\langle\lambda_2^3\right\rangle/\left\langle s_{ij}s_{ji}\right\rangle^{3/2}$ at x/x_*^{peak}=2.04 can explain why $\langle\omega_i s_{ij}\omega_j\rangle$ decays slower than $\left\langle s_{ij}s_{ji}\right\rangle^{3/2}$ (see table 8) from the peak station to this location.

In conclusion, $\langle\omega_i s_{ij}\omega_j\rangle$ and $-\langle s_{ij}s_{jk}s_{ki}\rangle$ decay slower than $\left\langle s_{ij}s_{ji}\right\rangle^{3/2}$ in the decay region because this is where the asymmetric structure of the velocity gradients is fully developing, translating into changes in the distribution of the eigenvalues, and because of the evolution in eigenvector alignments with vorticity. The next sub-sections are dedicated to the study of how the aforementioned asymmetry develops in terms of PDFs of $\omega_i s_{ij}\omega_j$, $s_{ij}s_{jk}s_{ki}$, λ_i and $\omega_i^2\lambda_i cos^2(\omega,e_i)$.

4.2. *Probability density functions of strain rate and enstrophy production*

Experimental and numerical observations (see Tsinober (2000) and references therein) show that vortex stretching ($\omega_i s_{ij}\omega_j > 0$) is favoured on average over vortex compression ($\omega_i s_{ij}\omega_j < 0$). Taylor (1938) was the first to conclude that $\langle\omega_i s_{ij}\omega_j\rangle$ is positive and Betchov (1975) presented the first PDFs of $\omega_i s_{ij}\omega_j$. Since then, several studies for different types of flow have been presented supporting Taylor's (1938) result such as Tsinober *et al.* (1992, 1995*b*) for grid turbulence and DNS of homogeneous isotropic turbulence, Tsinober *et al.* (1995*a*) for pipe flow, Kholmyansky *et al.* (2001) for the atmospheric surface layer, Buxton & Ganapathisubramani (2010) for the far field of a jet and now the present study for a spatially developing flow in the lee of a fractal grid (see table 6).

Figure 12 shows our PDFs of $\omega_i s_{ij}\omega_j$ and $s_{ij}s_{jk}s_{ki}$ normalized by $(U_\infty/x_*^{peak})^3$. The PDF of $\omega_i s_{ij}\omega_j$ has a symmetric appearance (though already slightly skewed to positive values if one looks at $\langle\omega_i s_{ij}\omega_j\rangle$ in figure 10 and table 6) at both x/x_*^{peak}=0.57 and 0.94. It becomes clearly asymmetric and skewed to positive values at x/x_*^{peak}=2.04 where also the width of the PDF reduces greatly.

The PDF of $s_{ij}s_{jk}s_{ki}$ has a slightly asymmetric appearance and very high fluctuations (both positive and negative) at x/x_*^{peak}=0.57 and 0.94. In the decay region these fluctuations are greatly reduced and the asymmetry to negative values of $s_{ij}s_{jk}s_{ki}$ is highly amplified. The tendency for positive self-amplification of strain ($s_{ij}s_{jk}s_{ki} < 0$) is present throughout and already in the production region. The tendency for vortex stretching ($\omega_i s_{ij}\omega_j > 0$) is not so evident (though slightly present) at the production

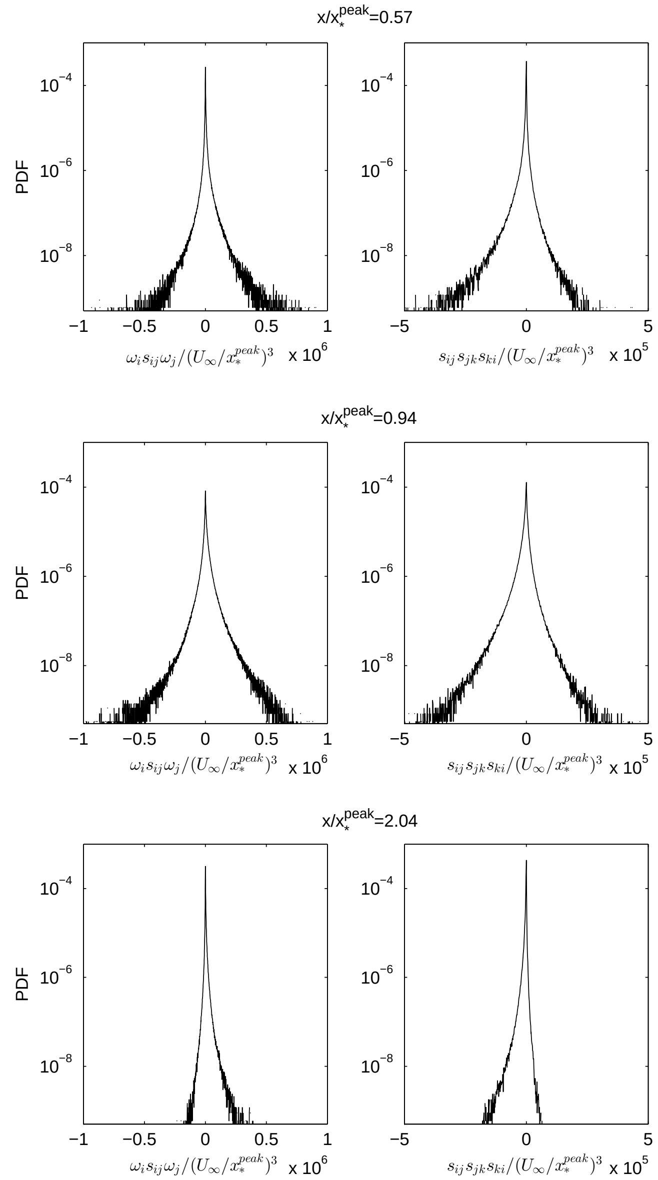

FIGURE 12. Probability density functions of enstrophy production rate $\omega_i s_{ij}\omega_j$ and strain production rate $s_{ij}s_{jk}s_{ki}$ normalized by $(U_\infty/x_*^{peak})^3$ at the three measured stations. Data conditioned to values where $|P| < 0.02(\nu/\eta^2)$

and peak stations which points to a particular importance of strain self-amplification in the generation of turbulence.

4.3. *Vortex stretching and compressing*

In table 8 the reference cases show that, at x/x_*^{peak}=0.57 and 0.94, the relative levels of average vortex stretching $\langle\omega_1^2\lambda_1 cos^2(\omega, e_1)\rangle$ and average vortex compressing $\langle\omega_3^2\lambda_3 cos^2(\omega, e_3)\rangle$ with respect to $\langle\omega_i s_{ij}\omega_j\rangle$ are high (174% more at x/x_*^{peak}=0.57 and 212% more for vortex stretching at x/x_*^{peak}=0.94 than in the reference grid turbulence case). That vortex compressing and vortex stretching should be high together follows from incompressibility. At x/x_*^{peak}=2.04 the values are comparable to the reference cases.

Note that the PDFs of figure 12 show highly enhanced presence of negative and positive values of $\omega_i s_{ij} \omega_j$, i.e. vortex compression and vortex stretching events, at x/x_*^{peak}=0.57 and 0.94 compared to our decay region station x/x_*^{peak}=2.04. This observation is aligned with the observation that at x/x_*^{peak}=0.57 and 0.94 there are much higher values of both λ_1 and λ_3 than in the other station (figure 14) and with the observation in figure 13 that at x/x_*^{peak}=0.57 and 0.94 there are much higher values of $\omega_i^2 \lambda_i cos^2(\omega, e_i)$ than in our decay station (figure 13).

Looking at the ratios $\left\langle \omega_1^2 \lambda_1 cos^2(\omega, e_1) \right\rangle / \left| \left\langle \omega_3^2 \lambda_3 cos^2(\omega, e_3) \right\rangle \right|$ (obtained from table 8) it is possible to measure the relative strength of average vortex stretching over average vortex compression. At x/x_*^{peak}=0.57 and 0.94 this ratio is around 1.2 whereas for the grid turbulence reference case and at x/x_*^{peak}=2.04 it is around 2.1. This fact agrees with the much stronger asymmetry seen at x/x_*^{peak}=2.04 in the plots of figure 12 than at x/x_*^{peak}=0.57 and 0.94. Figure 13 also confirms this tendency to asymmetry at x/x_*^{peak}=2.04 through the PDFs of $\omega_i^2 \lambda_i cos^2(\omega, e_i)$ (for i =1 to 3). It is important to highlight the large fluctuations at x/x_*^{peak}=0.57 and 0.94 when compared to x/x_*^{peak}=2.04. This fact explains the abnormally high ratios of $\left\langle \omega_1^2 \lambda_1 cos^2(\omega, e_1) \right\rangle / \langle \omega_i s_{ij} \omega_j \rangle$ and $\left\langle \omega_3^2 \lambda_3 cos^2(\omega, e_3) \right\rangle / \langle \omega_i s_{ij} \omega_j \rangle$ at the production and peak stations in relation to the decay region and reference cases (see table 8). It is also interesting to stress how the different results are at x/x_*^{peak}=0.57 and 2.04 as these two stations have similar PIV resolutions (see table 4) and similar values of Re_λ (see table 8), where $Re_\lambda = u'\lambda/\nu$, u' being the r.m.s. of the streamwise velocity fluctuation, $\lambda = \sqrt{\langle u^2 \rangle / \langle (\partial u / \partial x)^2 \rangle}$ the Taylor microscale and ν the kinematic viscosity.

4.4. *The extensive and compressive eigenvalues λ_1 and λ_3*

The PDFs of the eigenvalues are shown in figure 14 for our three stations. The PDFs of λ_1 and λ_3 are close to mirror images of each other at x/x_*^{peak}=0.57 and 0.94. Given (4.12) where the effects of λ_1 and λ_3 on $\omega_i s_{ij} \omega_j$ are linear in λ_1 and λ_3, this observation appears related to the symmetry of the PDF of $\omega_i s_{ij} \omega_j$ at the same two stations as shown in figure 12. This is not so for the effects of λ_1 and λ_3 on $s_{ij} s_{jk} s_{ki}$ which are not linear in λ_1 and λ_3 but equal to the third powers of these eigenvalues (see equation 4.11) implying that any residual breaking of the mirror symmetry between the PDFs of λ_1 and λ_3 is greatly amplified and yields an even stronger asymmetry in the PDF of $s_{ij} s_{jk} s_{ki}$. The PDF of $\omega_i s_{ij} \omega_j$ becomes clearly skewed at x/x_*^{peak}=2.04 (figure 12) and this is also where the approximate mirroring of the PDFs of λ_1 and λ_3 breaks down (figure 14). Note also that at x/x_*^{peak}=0.57 and 0.94 the extreme events have larger magnitudes than at the decay region station.

For x/x_*^{peak}=0.57 and 2.04 the tails of the PDFs of λ_1 and λ_3 are well fitted by an exponential function $e^{a \frac{\lambda_i}{U_\infty / x_*^{peak}}}$ (i =1 or 3) for almost 4 decades. The dimensionless factor a is 0.12 for the PDF of λ_3 and -0.14 for the PDF of λ_1 at x/x_*^{peak}=0.57, but 0.16 and -0.22 at x/x_*^{peak}=2.04 in agreement with the points made in the previous paragraph. The significant difference in the values of a for λ_1 in the production and decay regions indicates both stronger and many more strong stretching events at the production than in the decay region, and similarly for λ_3 and compression events.

Table 7 shows that the ratios between $\left\langle \lambda_i^3 \right\rangle$ (for i =1 to 3) and $-\langle s_{ij} s_{jk} s_{ki} \rangle = -\left\langle \lambda_1^3 + \lambda_2^3 + \lambda_3^3 \right\rangle$ are similar at x/x_*^{peak}=0.57 and 0.94 and differ from the ones at

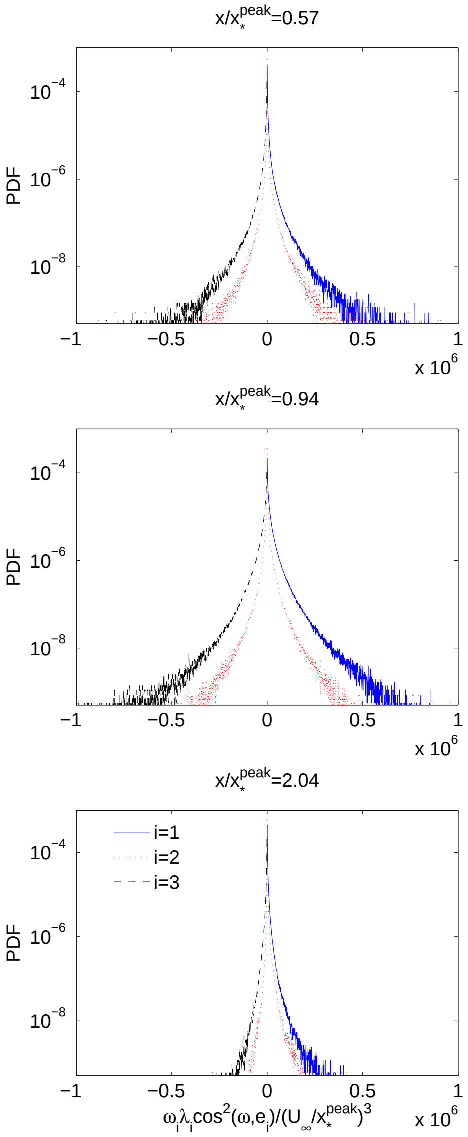

FIGURE 13. Probability density functions of the eigenvalue contribution to enstrophy production rate $\omega_i^2 \lambda_i cos^2(\omega, e_i)$ (for i =1 to 3) normalized by $(U_\infty/x_*^{peak})^3$ at the three measured stations. Data conditioned to values where $|P| < 0.02(\nu/\eta^2)$

x/x_*^{peak}=2.04. It seems that $\langle\lambda_i^3\rangle/{-\langle s_{ij}s_{jk}s_{ki}\rangle}$ (for i =1 to 3) are comparable to the field reference case only at x/x_*^{peak}=2.04 whereas at the two previous stations these ratios are much higher in amplitude. The extreme events and high fluctuations of λ_1 and λ_3 seen in their PDFs at x/x_*^{peak}=0.57 and 0.94 are the root of these abnormally high ratios.

Betchov (1956) showed that for homogeneous, isotropic flows the skewness of $\partial u/\partial x$ can be written as

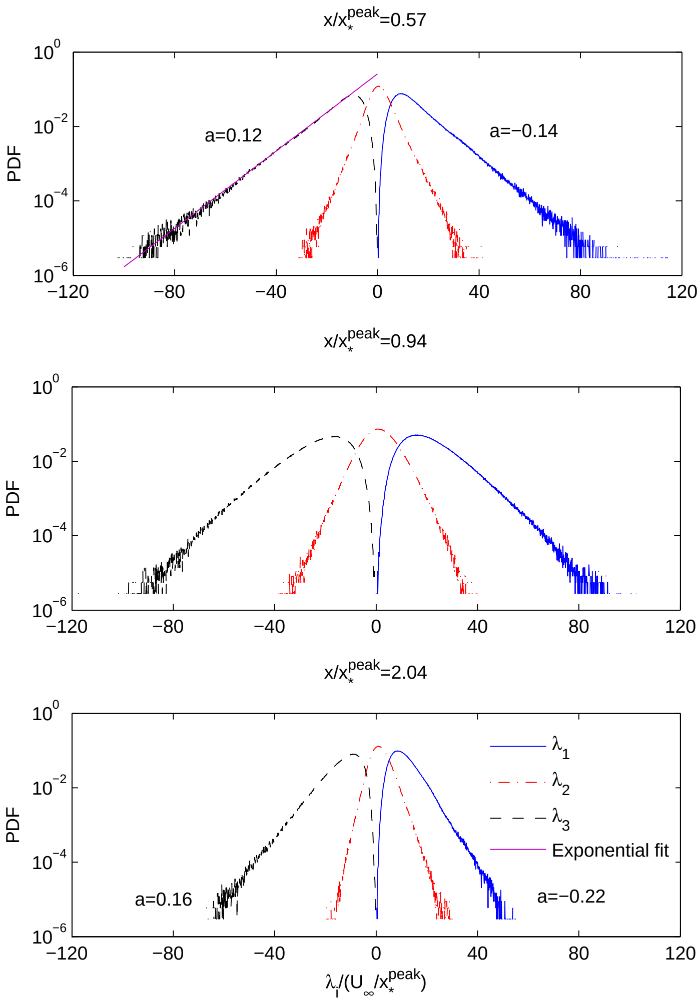

FIGURE 14. Probability density functions of the eigenvalues λ_i (i =1, 2 and 3) of the strain rate tensor plotted in linear-logarithmic axes for x/x_*^{peak} = 0.57, 0.94 and 2.04. The PDF tails at stations $x/x_*^{peak} = 0.57$ and 2.04 are fitted with exponential functions $\propto e^{a\frac{\lambda_i}{U_\infty/x_*^{peak}}}$ for i =1 or 3. The factor a for each tail is displayed in the plot where the coefficient of determination R^2 is larger than 0.99 for every calculated fit. Data conditioned to values where $|P| < 0.02(\nu/\eta^2)$

$$S = -\frac{\left\langle \left(\frac{\partial u}{\partial x}\right)^3 \right\rangle}{\left\langle \left(\frac{\partial u}{\partial x}\right)^2 \right\rangle^{3/2}} = -\frac{8}{105 \left\langle \left(\frac{\partial u}{\partial x}\right)^2 \right\rangle^{3/2}} \left(\langle \lambda_1^3 \rangle + \langle \lambda_2^3 \rangle + \langle \lambda_3^3 \rangle \right) \tag{4.13}$$

which clearly shows the contribution of $\langle \lambda_i^3 \rangle$ (i=1,2 and 3) to the calculation of S. Since $\langle \lambda_2^3 \rangle \approx 0$, the main contribution to S comes from $\langle \lambda_1^3 \rangle$ and $\langle \lambda_3^3 \rangle$. We do not use Betchov's (1956) formula to estimate S so as to not rely on his isotropy and homogeneity assumptions. Instead, we calculate S directly from the first (definition) equality in (4.13). For our three stations, S takes the values in table 9. Sreenivasan & Antonia (1997, pp. 453) show, through a compilation from several different sources (comprising homogeneous and

x/x_*^{peak}	0.57	0.94	2.04
S	0.082	0.178	0.260
Re_λ	271	364	257

TABLE 9. Values of the skewness of $\partial u/\partial x$ (S) and Re_λ for our measured stations.

inhomogeneous flows such as wakes, jets and boundary layers), that S seems to increase monotonically with Re_λ. However, stations located at x/x_*^{peak}=0.57 and 2.04 have similar Reynolds numbers (table 9) and yet, at x/x_*^{peak}=2.04, S is around 3.2 times the value at x/x_*^{peak}=0.57. In addition, S calculated at x/x_*^{peak}=2.04 and 0.94 decreases from 0.260 to 0.178 when Re_λ increases from 257 to 364, respectively. We also find that our values of skewness are lower than all of the data in Sreenivasan & Antonia (1997, pp. 453) (with the exception of only one data point) for similar and higher Reynolds numbers. These differences cannot be attributed to different experiment resolutions (table 4) or setups. Nevertheless, the existence of noise (as little as it may be) could affect the skewness as it is a third order moment of the velocity gradient. Equation 4.13 shows that the level of skewness of $\partial u/\partial x$ depends on how asymmetric the distribution of λ_1 is in comparison to λ_3 and, therefore, its evolution is in agreement with our previous discussion of figure 14.

4.5. *The intermediate eigenvalue* λ_2

So far, it has been seen that there are marked differences in the stretching and compressive eigenvalues at our measured stations. However, looking at table 7 the second eigenvalue normalised by $-\langle s_{ij}s_{jk}s_{ki}\rangle$ does not seem to be significantly different across all stations in the present study and when compared to our reference cases. We therefore now focus our analysis on this particular eigenvalue.

Depending on the sign of λ_2 the local flow adopts different topologies. If λ_2 is positive there are two stretching directions and the flow behaves locally like a jet parallel to e_3 and impinging on a wall on the e_1e_2 plane (sheet-like structures). If λ_2 is negative the flow behaves locally as if entering a contraction cone (tube-like structures). Betchov (1956) showed that the process of enstrophy production and energy transfer should be mostly related, in an average sense, to the former.

In figure 14 the PDFs of λ_2 resemble closely the behaviour of the PDFs of $\omega_i s_{ij}\omega_j$ (figure 12); namely, they look symmetric at x/x_*^{peak}=0.57 and 0.94 and then become clearly skewed at x/x_*^{peak}=2.04.

Following Ashurst *et al.* (1987) we define a normalized second eigenvalue as $\lambda_2^* = \sqrt{6}\lambda_2/\sqrt{\lambda_1^2+\lambda_2^2+\lambda_3^2}$. Figure 15 shows the joint PDFs of λ_2^* and $-Q_s$ (strain) or Q_ω (enstrophy) at x/x_*^{peak}=0.94 and 2.04 (these joint PDFs are similar at x/x_*^{peak}=0.57 and 0.94). The values of λ_2^* are bounded by ±1.5 due to the divergence error (for incompressible flow they must be bounded by ±1). Nevertheless, the conclusions taken from these joint PDFs are related to areas where Q_s and Q_ω are large and it is shown in figure 31 of appendix A that the divergence error in these areas is small. In terms of the behaviour of λ_2^* with respect to $-Q_s$, for areas with high strain there is a tendency at x/x_*^{peak}=2.04 for λ_2^* to be close to 0.5, which is consistent with the observations of Ashurst *et al.* (1987) and Ganapathisubramani *et al.* (2008). If $\lambda_2^* > 0$ then $-s_{ij}s_{jk}s_{ki} = -3\lambda_1\lambda_2\lambda_3 > 0$ (see (Betchov 1956)) which contributes positively to strain production as seen in equation 4.8. On the other hand, at x/x_*^{peak}=0.94, λ_2^* is only marginally positive for large $-Q_s$ and similar conclusions can be drawn from figure 15 in terms of Q_ω rather than $-Q_s$.

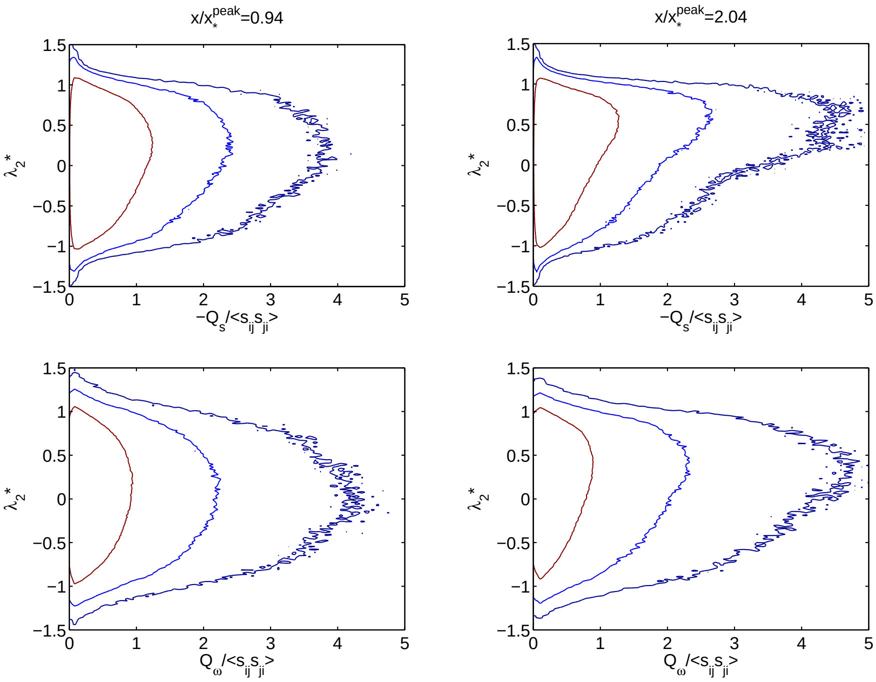

FIGURE 15. Joint probability density function of the normalized second eigenvalue λ_2^* and $-Q_s$ (strain) and Q_ω (enstrophy) at x/x_*^{peak}=0.94 and 2.04. Iso-countours range from 10^{-1} to 10^{-3}. Data conditioned to values where $|P| < 0.08(\nu/\eta^2)$.

The joint PDFs of λ_2^* and Q_ω are clearly more symmetric about the $\lambda_2^* = 0$ axis at x/x_*^{peak}=0.94 and 0.57 than at x/x_*^{peak}=2.04: at x/x_*^{peak}=0.94 and 0.57, there is no preference for sheet or tube-like structures in high enstrophy regions in the sense that λ_2^* has equal probability of being positive or negative.

4.6. *Kolmogorov 2/3 scaling*

It can be argued that vortex stretching/compression and strain self-amplification/reduction are related to interscale energy transfer. Tennekes & Lumley (1972) argue that vortex stretching is responsible for transferring energy from large to small scales. On the other hand, Tsinober (2009) argues that vortex compression and strain self-amplification (which contribute positively to the increase in fluctuating strain in the flow as seen in equation 4.8) is the mechanism that aids the formation of a cascade because strain dominated regions appear to be most active and nonlinear in the flow. Irrespective of what the actual velocity gradient amplification mechanism is, interscale energy transfer results in the excitation of a range of turbulent scales characterised by a power law range in the energy spectrum or in its counterpart in physical space, the second order structure function. Figure 16a shows the second order structure function $\langle \delta u^2(r) \rangle$ at x/x_*^{peak}=0.94 where $\delta u = u(x+r) - u(x)$ is computed in terms of the streamwise fluctuating velocity component $u(x)$ in the streamwise direction x. This structure function is evaluated in the volume reconstructed from Taylor's hypothesis where the average is taken over all three spatial directions. We use the Kolmogorov velocity $u_k = (\nu\epsilon)^{1/4}$ and the Kolmogorov length scale $\eta = (\nu^3/\epsilon)^{1/4}$ to normalize the structure function and the distance r, respectively. For small r, $\langle \delta u^2(r) \rangle$ follows the power law exponent 2 indicating that the dissipative scales are well captured with the present experimental resolution. In addition,

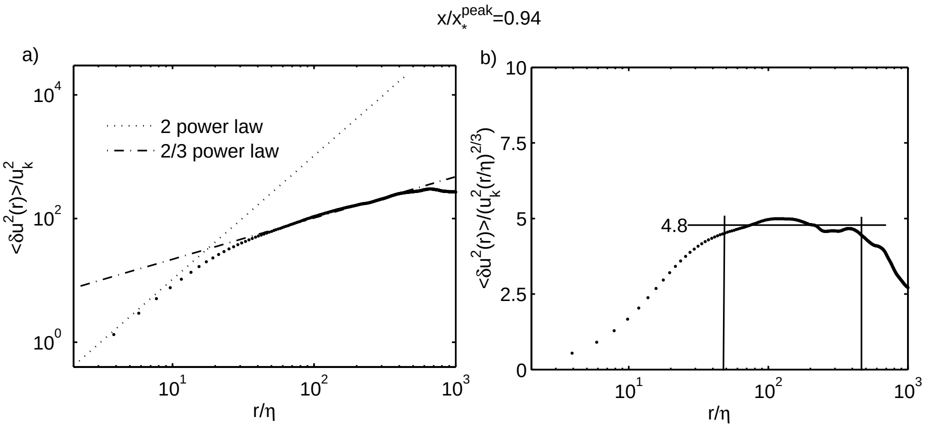

FIGURE 16. a) Second order structure function evaluated at $x/x_*^{peak} = 0.94$ where $Re_\lambda = 364$ (see table 8) and b) the same data as in a) but compensated with $(r/\eta)^{2/3}$ and plotted in a linear-logarithmic axis. The power law plateau in b) is attained within a deviation of 5% from the mean value of 4.8 within the r/η range indicated. $\langle \delta u^2(r) \rangle$ is evaluated over a fixed volume of 150 × 80 × 2726 points in the y, z and x (via Taylor's hypothesis) directions, respectively, which means that the smaller separations are statistically better converged than the larger ones. The Kolmogorov velocity (u_k) and length (η) scales used to normalise the data in the figure are computed over the whole volume domain.

figure 16a shows that $\langle \delta u^2(r) \rangle$ adopts a power law range with a power law exponent close to Kolmogorov's 2/3 over a decade. Figure 16b shows this power law in linear-logarithmic axes to better detail its accuracy.

The Kolmogorov scaling $\langle \delta u^2(r) \rangle \propto r^{2/3}$ is present in a region where the vortex stretching only slightly dominates over compression, where they both fluctuate to high values (see the PDFs of λ_1, λ_2 and λ_3 in figure 14, the PDFs of $\omega_i s_{ij} \omega_j / \langle s_{ij} s_{ji} \rangle^{3/2}$ in figure 12, the PDFs in figure 13 and table 8) and where there is only marginal preference for sheet-like over tube-like structures in the sense of the average sign of λ_2^* (see the behaviour of λ_2^* with $-Q_s$ and Q_ω in figure 15). We study the behaviour of the structure function $\langle \delta u^2(r) \rangle$ in more depth in section 5. Before that, we report in the following subsection on $Q - R$ statistics.

4.7. *Joint PDFs of invariants*

We have shown, in terms of various statistics of the velocity gradient tensor, that our flow is similar to previous studies only at our decay region station. It is fair to ask if other signatures of the velocity gradient tensor behave similarly.

The invariants Q and R defined by equations 4.1 and 4.2 are useful quantities to study turbulence structure. Chacin & Cantwell (2000) suggested that the joint PDF of these quantities (the $Q - R$ diagram) has an universal "tear-drop" shape. Tsinober (2009) compiled data from different turbulent flows such as boundary layers, mixing layers, grid turbulence and jet turbulence showing that they all, indeed, share the same shape.

Following Laizet *et al.* (2013) we present in figure 17 the spatial evolution of the $Q-R$ diagram for the three stations studied. To the best of our knowledge, this is the first time that a spatial development of these invariants is presented from experimental data. The x/x_*^{peak}=2.04 station is located in a region where Seoud & Vassilicos (2007), Mazellier & Vassilicos (2010), Valente & Vassilicos (2011), Valente & Vassilicos (2012), Gomes-

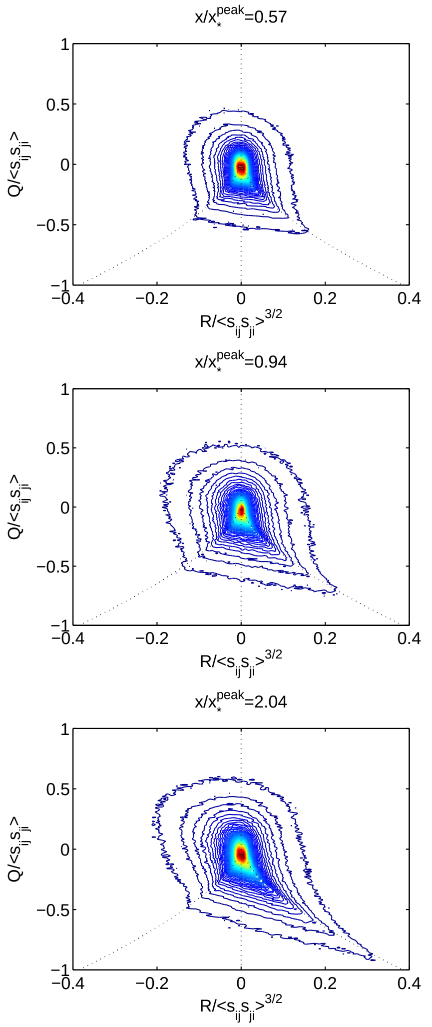

FIGURE 17. Joint probability density function of the second (Q) and third (R) invariants of the velocity gradient tensor. Iso-countours range from 10^0 to 10^{-2}. Data conditioned to values where $|P| < 0.02(\nu/\eta^2)$.

Fernandes *et al.* (2012), Discetti *et al.* (2013) and Nagata *et al.* (2013) showed that the dimensionless dissipation constant varies along the streamwise direction like $C_\epsilon \propto Re_\lambda^{-1}$ even though the turbulence is well-developed in the sense that it has Gaussian fluctuating velocities and the energy spectra have broad power laws with exponents very close to -5/3. Yet, the $Q-R$ diagram is similar to the classical "tear-drop" shape at this station.

The classical "tear-drop" shape of the $Q-R$ diagram tells us that in regions where strain dominates ($Q < 0$) it is most probable that $R > 0$, i.e., that the production of $1/2s_{ij}s_{ij}$ is greater than the production of $1/4\omega_i\omega_i$, and that in regions where enstrophy dominates ($Q > 0$) it is more probable that $R < 0$. This fact gives rise to the typical tail shape of the diagram. Nevertheless, at x/x_*^{peak}=0.57, there is an almost equal probability that enstrophy dominated regions are producing velocity gradients of the strain ($R > 0$) or vorticity ($R < 0$) type. At x/x_*^{peak}=0.94, the station located close to the turbulence intensity peak, there is a transitional shape where a more pronounced tail is noticeable

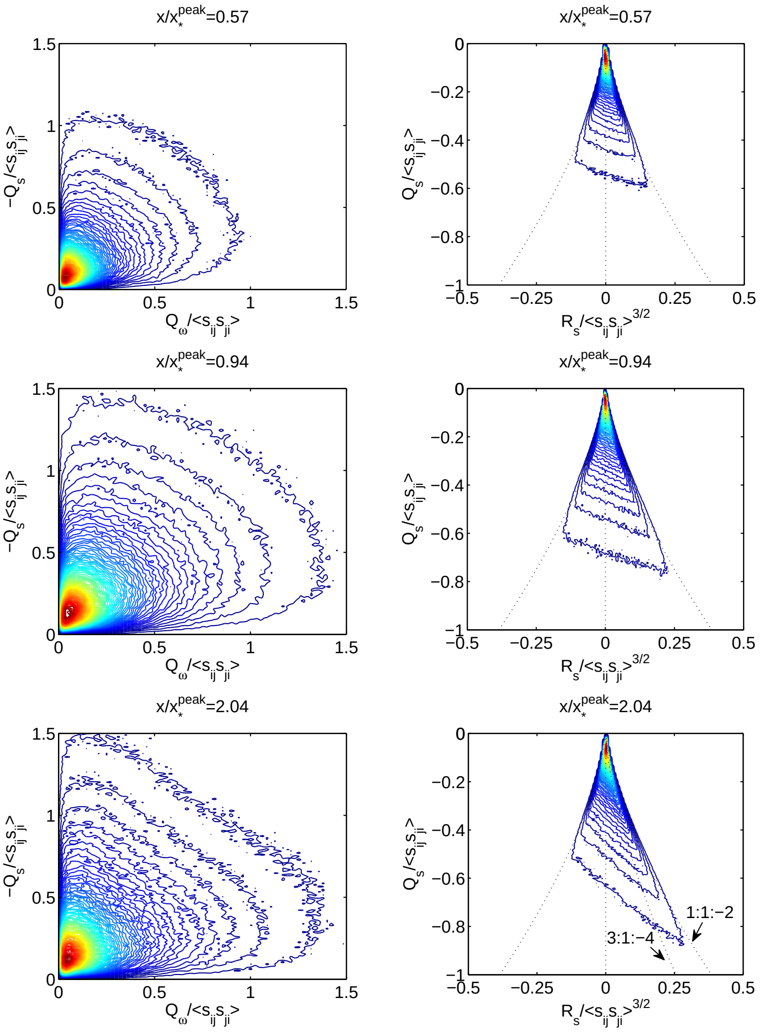

FIGURE 18. Joint probability density functions of $-Q_s$ and Q_ω and Q_s and R_s for all measured stations. Iso-countours range from 10^0 to 10^{-2}. Data conditioned to values where $|P| < 0.02(\nu/\eta^2)$.

than at x/x_*^{peak}=0.57 and larger velocity gradients appear. However, this is also the station where the PDFs of $\omega_i s_{ij} \omega_j$ and $s_{ij}s_{jk}s_{ki}$ are the broadest and least skewed (see figure 12).

Figure 18 shows the joint PDFs of $-Q_s$ and Q_ω. For every station measured, the lowest probability iso-contour (10^{-2}) shows a maximum value of Q_ω which is similar to the maximum value $-Q_s$ on that same iso-contour. Furthermore, regions where there is a large value of $-Q_s$ are most probably associated with a low value of Q_ω and vice-versa. In order words, it is probable that large values of $-Q_s$ are in regions of high strain and low enstrophy and that large values of Q_ω are in regions of high enstrophy and low strain (see Soria *et al.* (1994, p. 873) for a physical interpretation of joint PDFs of $-Q_s$ and Q_ω). If more points are taken into account, thereby reducing the correlation coefficient between $\partial u/\partial x$ and $-(\partial v/\partial y + \partial w/\partial z)$ but also lowering the probability contours, the same behaviour is found.

It seems that the behaviour of the joint PDF of $-Q_s$ and Q_ω is largely dependent on the type of turbulent flow. For the homogeneous isotropic turbulence DNS of Ooi *et al.* (1999), the peak value of Q_ω attains larger values than the peak value of $-Q_s$ within the same probability contour. In the log-law and wake regions of the channel flow simulations of Blackburn *et al.* (1996), the peak value of $-Q_s$ is larger than the peak value of Q_ω for each probability contour. In Chong *et al.* (1998), a simulation of a boundary layer is studied. In the wake region the PDF of $-Q_s$ and Q_ω is similar to what was found by Ooi *et al.* (1999) for homogeneous isotropic turbulence. However, in the log-law region, the joint PDF shape is a transition between a vortex sheet-like structure (see Soria *et al.* (1994, p. 873)) where $-Q_s$ is correlated to Q_ω in a diagonal line region in the buffer layer and what is seen in the wake region. In the DNS of time-developing mixing layers by Soria *et al.* (1994), the authors initialized the flow using a laminar error function with small disturbances in one case and two turbulent boundary layers with opposite freestream velocities in the other. Results showed that regions where $\langle \lambda_2^3 \rangle$ is positive (i.e. of vortex sheet-like structure), regions where $\langle \lambda_2^3 \rangle$ is negative (i.e. of vortex tube-like structure) or both can appear. These examples show that the information presented in the $Q-R$ diagram is not enough to characterize turbulent flow since the apparent similar "tear-drop" hides important information about the turbulence structure.

In terms of the joint PDF of Q_s and R_s, figure 18 presents another way of visualizing the behaviour of the second eigenvalue of the strain rate tensor given the relationship $R_s = -1/3 s_{ij} s_{jk} s_{ki} = -\lambda_1 \lambda_2 \lambda_3$ which means that R_s takes the sign of λ_2. In the stations x/x_*^{peak}=0.57 and 0.94,there is only slightly more probability of finding sheet-like structures than tube-like ones (see figure 15) in the sense that the probability of λ_2 being positive (sheet-like structures) is marginally larger than being negative (tube-like structures). This implies that, at those locations, the probability of finding $R_s > 0$ is slightly bigger than finding $R_s < 0$ and the joint PDF of Q_s and R_s is slightly tilted towards $R_s > 0$ as seen in figure 18. At x/x_*^{peak}=2.04, the evolution of the joint PDF of Q_s and R_s attains, at least qualitatively, the usual shape seen in mixing layers (Soria *et al.* 1994), channel flow (Blackburn *et al.* 1996), log-law and wake regions of boundary layers (Chong *et al.* 1998) and homogeneous isotropic turbulence (Ooi *et al.* 1999). For high strain regions (hence large negative values of Q_s), the ratio between the principal strain rates tends to follow slightly better the relation 1:1:-2 than the 3:1:-4 found by Ashurst *et al.* (1987). Cantwell (1992) proved analytically that for the restricted Euler equation the initial conditions determine this ratio between the principal strain rates. This fact and the results reported both here and in the literature suggest that this ratio should not be universal.

5. Instantaneous results and second order structure functions

5.1. *Structure function scaling and intermittent velocity and vorticity structures*

We saw in subsection 4.3 that $\langle \delta u^2(r) \rangle \propto r^{2/3}$ over more than a decade in a region of the flow (the peak of turbulent kinetic energy) where vortex stretching $\omega_1^2 \lambda_1 cos^2(\omega, e_1)$ nearly balances (in fact only slightly exceeds) vortex compression $\omega_3^2 \lambda_3 cos^2(\omega, e_3)$ on average. At this region and in the production one we found high vortex compression and strong strain self-reduction events (figure 12) as well as the most extreme values of λ_1 and λ_3 (figure 14). The turbulence behaves as usually reported in terms of statistics of velocity fluctuation gradients only further downstream, in the decay region, where the extreme events of enstrophy production and strain rate are smaller and strongly skewed toward vortex stretching and strain self-amplification, respectively.

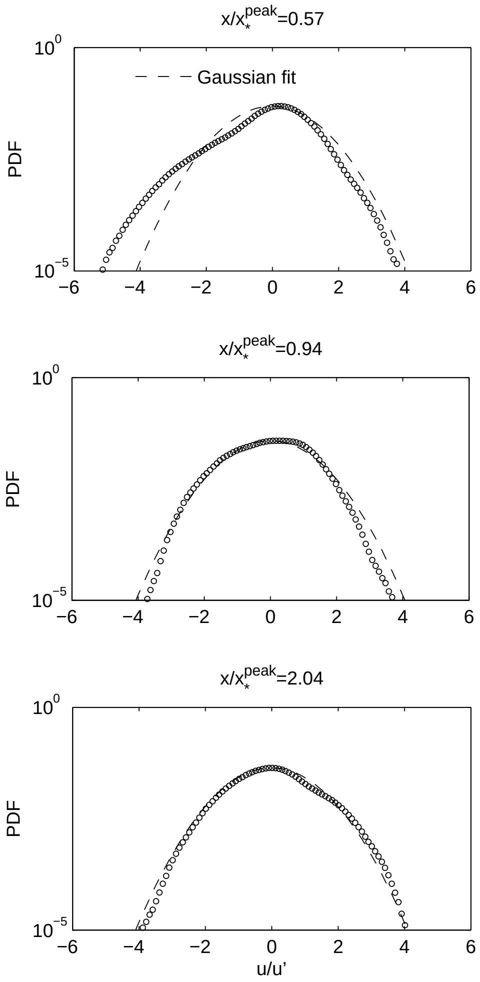

FIGURE 19. PDFs of the streamwise velocity fluctuation (u) normalized by its r.m.s. at x/x_*^{peak}=0.57, 0.94 and 2.04.

In fact, the velocity fluctuations are not even fully gaussian at the turbulence peak station (where $\langle\delta u^2(r)\rangle \propto r^{2/3}$), and they are even less gaussian at the production region. Figure 19 shows the PDFs of the normalised velocity fluctuation component in the streamwise direction (u/u') at x/x_*^{peak}=0.57, 0.94 and 2.04. Data are collected from the temporal information of the velocity field across the yz area of measurement at these streamwise locations. The PDF of velocity fluctuations is best fitted by a gaussian (the velocity fluctuations are therefore the least intermittent) at x/x_*^{peak}=2.04, i.e. the station in the decay region.

The second order structure function $\langle\delta u^2(r)\rangle$ has a well-defined $r^{2/3}$ scaling over slightly more than a decade at the x/x_*^{peak}=0.94 location (figure 16) where $Re_\lambda = 364$ and at x/x_*^{peak}=2.04 (figure 20b) where $Re_\lambda = 257$ but does not present a significant 2/3 power law range at the production region station (figure 20a) where Re_λ (=271) is comparable to Re_λ (=257) in the decay region station. The production region is where not

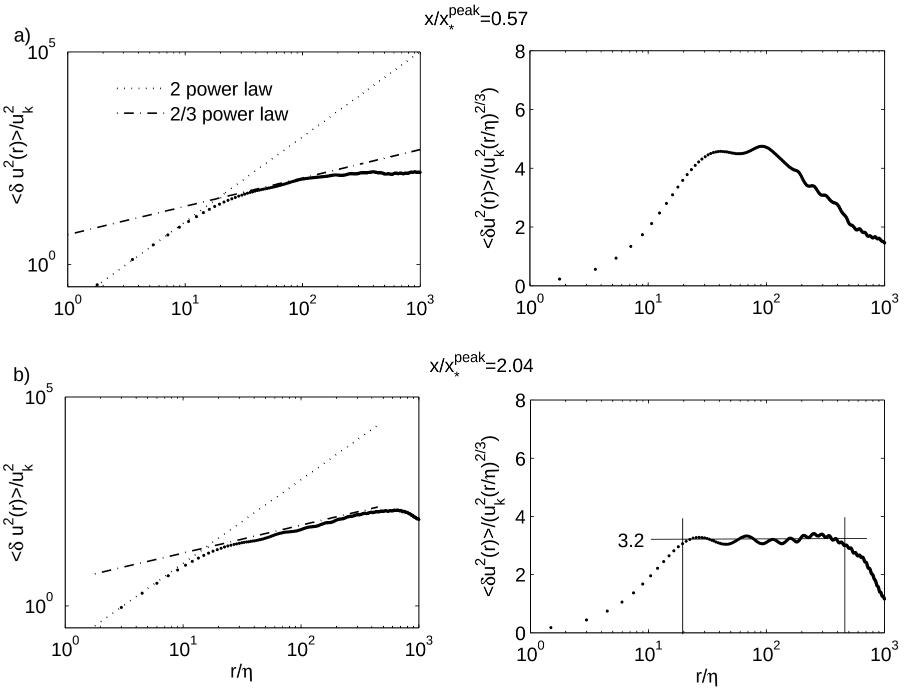

FIGURE 20. Second order structure function (left) and compensated with $(r/\eta)^{2/3}$ and plotted in a linear-logarithmic axis (right) evaluated at a) x/x_*^{peak}=0.57 ($Re_\lambda = 271$) and b) x/x_*^{peak}=2.04 ($Re_\lambda = 257$). The power law plateau in b) is attained within a deviation of 6% from the mean value of 3.2 within the r/η range indicated. The Kolmogorov velocity (u_k) and length (η) scales used to normalise the data in the figure are computed over the whole volume domain at each station.

only the velocity fluctuations (figure 19) but also the enstrophy field are most intermittent. Figure 21 shows the iso-surfaces of enstrophy corresponding to 8% of the maximum enstrophy present at x/x_*^{peak}=0.57 and a zoomed in view of a very active sub-region. The intermittency in the spatial distribution of enstrophy bundles is clear in figure 21. The statistical result plotted in figure 15 shows that for high enstrophy regions there is no preference for tube or sheet-like structures can be visually confirmed here in the zoomed-in version of the enstrophy contours. The x direction is reconstructed using Taylor's hypothesis (see section 3) and therefore should be interpreted as time information converted into space. If the threshold is increased to a larger percentage of the maximum enstrophy, the location of the iso-surfaces remains similar to the present ones but with more intermittency.

5.2. *Assessment of turbulent sub-regions*

We now concentrate attention on our production region station x/x_*^{peak}=0.57 where, because of the very pronounced intermittency (figure 21), it is possible to study the r-scalings of $\langle \delta u^2(r) \rangle$ (where $\delta u(r) = u(x+r) - u(x)$ and u is the streamwise fluctuating velocity component) in clearly different sub-regions of the flow.

In order to assess sub-regions of the flow, we follow the same approach as Mouri *et al.* (2008) and evaluate the second order structure function in smaller regions. One important

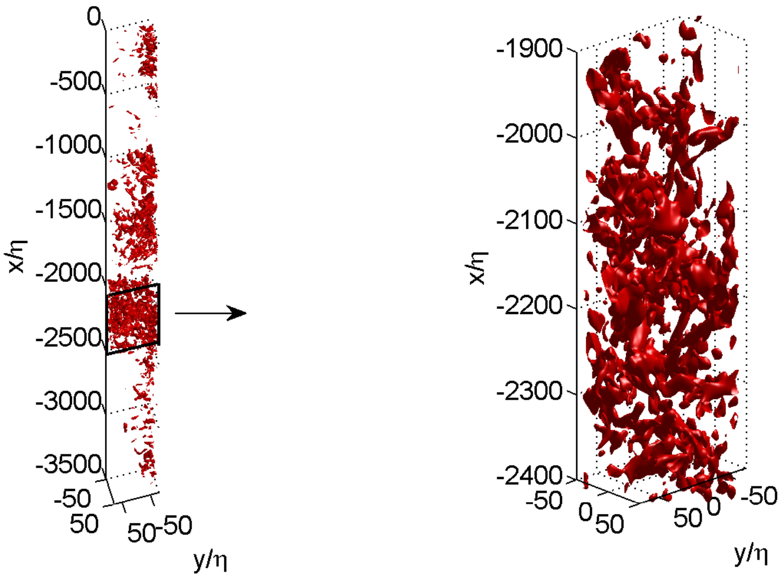

FIGURE 21. Iso-surfaces of enstrophy, $\omega^2 = 190 sec^{-2}$, which are approximately 8% of the maximum enstrophy at x/x_*^{peak}=0.57.

difference from Mouri *et al.* (2008) is that instead of averaging over one linear dimension we average over y, z and x within the considered sub-volume. The streamwise dimension of these sub-regions is estimated to be larger than the integral length scale L of u in the x direction. At x/x_*^{peak}=0.57 and for the Re_{t_0} of the present experiment (see table 2), $L/\eta \approx 270$ (data from Gomes-Fernandes *et al.* (2012)). We chose sub-volumes with a streamwise size of approximately 500η. For each sub-volume, the local Kolmogorov velocity $u_k = (\nu\epsilon)^{1/4}$ and length $\eta = (\nu^3/\epsilon)^{1/4}$ were computed by averaging over this sub-volume and the data were normalised with these locally obtained Kolmogorov scales.

One might expect a larger range of excited scales and a broader 2/3 power law in more active flow regions such as the region $-2550 < x/\eta < -2050$ (the zoomed-in view in figure 21). However, figure 22b shows that there is no significant change in this sub-region from the structure function computed for the entire volume (figure 22a).

To develop a systematic method of determining if there are regions where a broad 2/3 power law exists, an algorithm was developed and implemented. For a volume length of 500η it scans every x/η and estimates for $r > 30\eta \approx \lambda$ which power law exists and what is its range in the domain x/η to x/η+500. This algorithm consists of applying a threshold based on the coefficient of determination R^2 of a line fitted to the $log(\langle\delta u^2(r)\rangle)$ versus $log(r)$ data for increasing ranges of the two-point distance r. Initially three neighbouring values of r are considered all such that $r > 30\eta \approx \lambda$ and R^2 is computed. If R^2 is above a threshold, which was set to 0.97, another larger value of r is added to the dataset, hence considering a slightly larger range of r values, and the operation is repeated until the threshold criterion is not met. Whenever this happened it was considered that the power law range was over. Figure 23 shows the result of this algorithm. The threshold for R^2 was varied to check that results are very similar in terms of power law exponents detected. However, the ranges over which these power laws were defined turned out to be sensitive to the threshold. For instance, in the region $-3500 < x/\eta < -3000$ where the power law exponents seen in figure 23 seem to be valid as mere tangents, these power

a) Entire volume

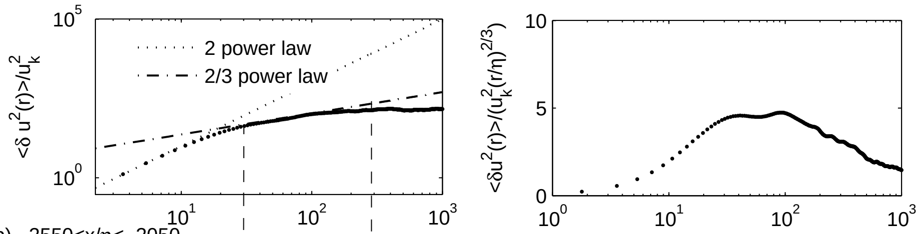

b) −2550<x/η<−2050

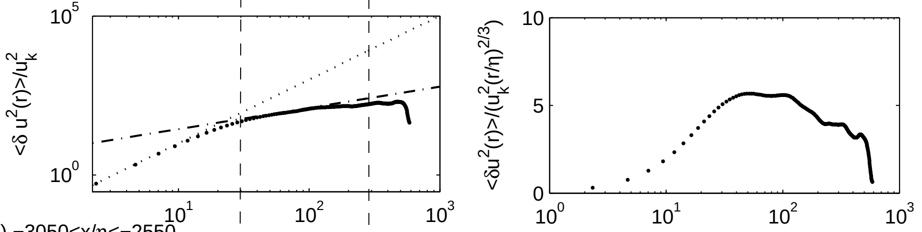

c) −3050<x/η<−2550

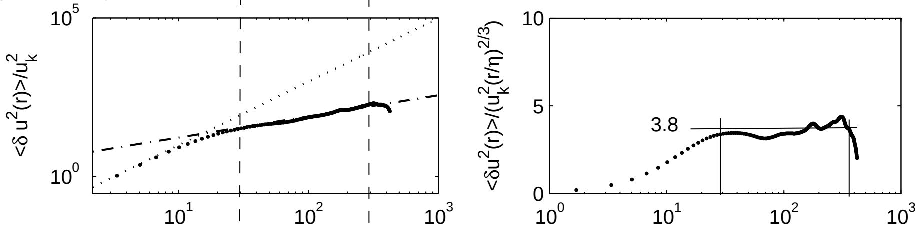

d) −3050<x/η<−2550 evaluated with half of the points

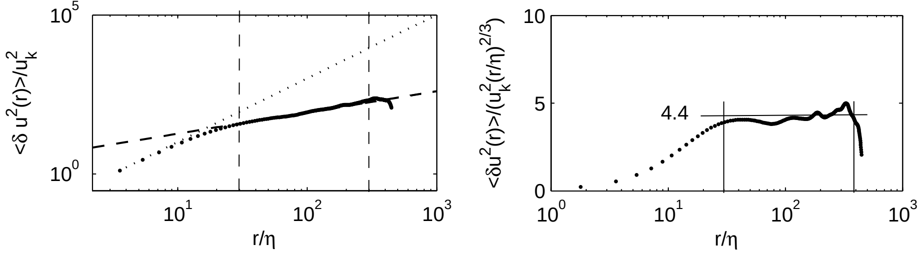

FIGURE 22. Second order structure function (left) and compensated with $(r/\eta)^{2/3}$ and plotted in a linear-logarithmic axis (right) evaluated in a) entire volume, b) $-2550 < x/\eta < -2050$, c) $-3050 < x/\eta < -2550$ and d) $-3050 < x/\eta < -2550$ with half of the points as in case c) (see figure 21) at x/x_*^{peak}=0.57. The power law plateaus in c) and d) are attained in the r/η range indicated within a deviation of 18% and 16% from the mean values of 3.8 and 4.4, respectively. The Kolmogorov velocity (u_k) and length (η) scales used to normalise the data in the figure are computed over each sub-volume domain.

laws could in fact be made to fit over a wider range of r with slightly lower threshold R^2 values.

Note that the general solution of the self-similar equation

$$F(\lambda x) = \gamma F(x) \tag{5.1}$$

where λ and γ are constants, is

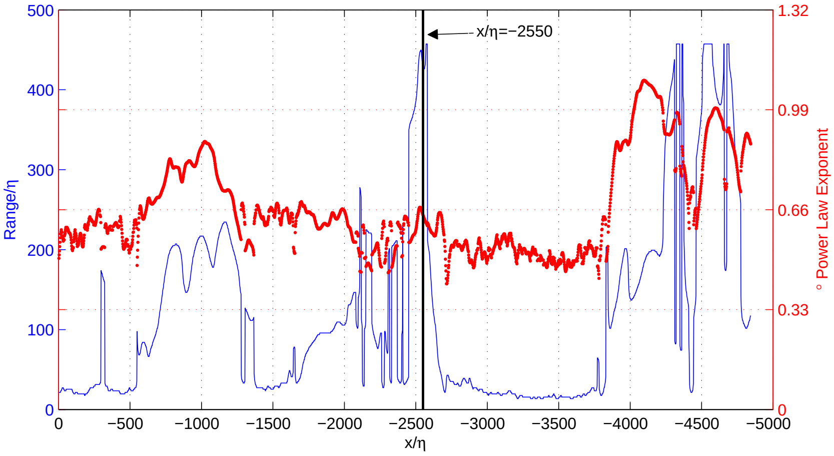

FIGURE 23. Range of values of r (thin continuous line) and power law exponent p (closed circles often appearing as a thick line) for $\langle \delta u^2(r) \rangle \propto r^p$. A 500η volume length in the streamwise distance was used for each x/η of the entire reconstructed volume at x/x_*^{peak}=0.57. The power law exponents are estimated from a line fitting with a coefficient of determination R^2 equal to 0.97. The vertical line at $x/\eta = 2550$ shows the location of the volume used to compute the structure function in figure 22b.

$$F(x) = x^\alpha P(ln(x)/ln(\lambda)) \tag{5.2}$$

where $\alpha = ln(\gamma)/ln(\lambda)$ and P is a periodic function of period 1. The oscillations in equation 5.2 can make it difficult to detect the range where the power law x^α holds, and it is fair to say that we do see what may be oscillations superimposed on some of our power laws (see figure 20b plotted in linear-logarithmic axis for an example of this phenomenon). Statistical convergence could also contribute to these oscillations and to the difficulty in detecting the power law exponents as well as their ranges. Nevertheless, our algorithm allowed us to identify, for example, that at $x/\eta = -2550$ (vertical line indicated in figure 23), there is a broad 2/3 power law range over a range of scales r between 30η and 450η (see figure 22c). Another interesting fact in figure 23 is that there exist various power laws with various scalings often different from Kolmogorov's 2/3.

Figure 22c shows that at $-3050 < x/\eta < -2550$ the second order structure function scales as $r^{2/3}$ over more than one decade (in figure 22d the same sub-region is used but $\langle \delta u^2(r) \rangle$ is evaluated with half the points used for figure 22c to test for statistical convergence). The fact that the sub-region $-3050 < x/\eta < -2550$ is less active in terms of vorticity than $-2550 < x/\eta < -2050$ (see figure 21) does not mean that broad 2/3 power laws only appear in regions with lower levels of enstrophy. One of our runs in the production station x/x_*^{peak}=0.57 was taken for case C (see table 2). In that run a broad 2/3 power law region was found in a very active region in terms of enstrophy (see figure 24).

x/x_*^{peak}=0.57 is the only region studied here where, using the aforementioned algorithm in sub-volumes of the flow, we can find a broader 2/3 power law (among other power laws) than the one estimated using the whole volume. The 2/3 power laws found in sub-volumes at the turbulence peak and decay stations have similar or smaller ranges than the ones computed using their entire volume.

Laizet *et al.* (2013) argued that the conditions at x/x_*^{peak}=0.57 for the validity of the

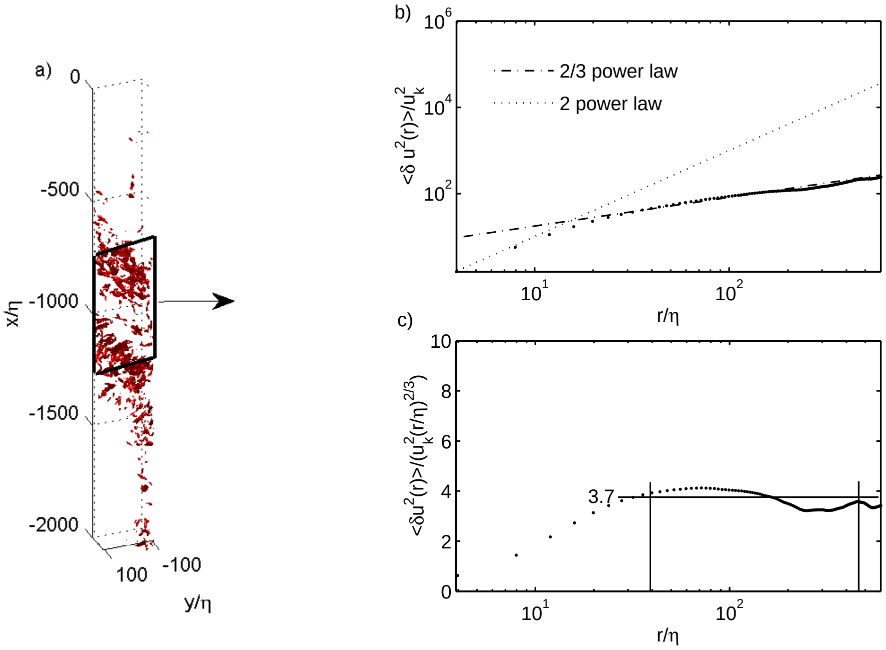

FIGURE 24. a) Iso-surfaces of enstrophy, $\omega^2 = 3170 sec^{-2}$, which are approximately 8% of the maximum enstrophy at x/x_*^{peak}=0.57 for case C ($Re_\lambda = 465$) (see table 2), b) second order structure function evaluated in the volume highlighted by the box and c) the same data as in b) but compensated with $(r/\eta)^{2/3}$ and plotted in a linear-logarithmic axis. The power law plateau in c) is attained within a deviation of 12% from the mean value of 3.7 in the r/η range indicated. The Kolmogorov velocity (u_k) and length (η) scales used to normalise the second order structure function are also computed over the volume highlighted by the box.

universal equilibrium Kolmogorov theory are not present. In their case, the DNS returns a clear 2/3 power law at such a point in the production region for the entire data, not just a sub-region even though their Reynolds numbers are much lower, in particular $Re_\lambda \approx 50$ at x/x_*^{peak}=0.57. However, their fractal grid-generated turbulent flow is different from the present one because of the significant background turbulence reported by Gomes-Fernandes *et al.* (2012) which is absent in their simulations. It is potentially interesting that this background turbulence might in fact be suppressing the 2/3 power law in the production region near the grid rather than enhancing it.

It is worth checking at this point if the sub-regions of clear 2/3 power law exponents at x/x_*^{peak}=0.57 are characterised by "tear-drop" shaped $Q-R$ diagrams even though the entire data set is not (see figure 17). Figure 25 shows the $Q-R$ diagram for the sub-region $-3050 < x/\eta < -2550$ of x/x_*^{peak}=0.57 where a broad 2/3 power law is found (see figure 22c). There is no striking difference between this diagram and the one seen in figure 17 for the same station. It could have been argued that, at x/x_*^{peak}=0.57, the unusual shape of the $Q-R$ diagram results from the small-scale intermittency which is clear in figure 21. However, the shape of the $Q-R$ diagram remains unchanged in the very active sub-region $-2550 < x/\eta < -2050$ (see figure 21). Hence, we conclude, that the absence of a tear drop Q-R shape at x/x_*^{peak}=0.57 is not caused by intermittency between highly vortical and weakly vortical regions and that sub-regions where $\langle \delta u^2(r) \rangle \propto r^{2/3}$ over a decade are not characterised by a "tear-drop" Q-R shape of their own.

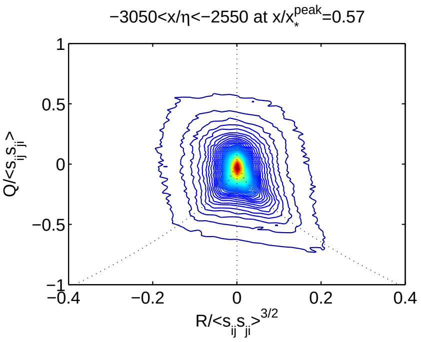

Figure 25. $Q-R$ diagram in the sub-region $-3050 < x/\eta < -2550$ at x/x_*^{peak}=0.57. Countours range from 10^0 to 10^{-2}. Data conditioned to values where $|P| < 0.08(\nu/\eta^2)$.

However, there are differences found in this sub-region of clear 2/3 power law exponent in comparison to the whole volume. The PDFs of $\omega_i s_{ij}\omega_j / \langle s_{ij}s_{ij}\rangle^{3/2}$ and $s_{ij}s_{jk}s_{ki} / \langle s_{ij}s_{ij}\rangle^{3/2}$ are found to be narrower than the whole volume (figure 12a shows the PDFs for the whole volume at x/x_*^{peak}=0.57) which means that less extreme events are captured. The same conclusion is found when looking at the PDF of the eigenvalues for this sub-region in comparison to the whole volume. It can be argued it happens because extreme events are rare and therefore more difficult to be found in smaller regions. Yet, the same procedure is applied in the sub-region of case C seen in figure 24a where the inlet velocity is greater; the same behaviour is found even though this is a high vortical region where more extreme events should, in principle, be easier to find. Kholmyansky & Tsinober (2009) looked at the scaling of structure functions of order p (where p=2 to 8 in increments of 1) and observed that if strong dissipative events were to be neglected from their calculations then the structure function scalings were very close to Kolmogorov $p/3$. It could be that the quality of the 2/3 power law scaling is improved in regions where intermittency is low.

5.3. *Assessment of the sub-region with a clear 2/3 power law exponent of* $\langle \delta u^2(r)\rangle$

We now analyse in more detail the sub-region $-3050 < x/\eta < -2550$ around x/x_*^{peak}=0.57 in the production region where a broad 2/3 power law is found (see figure 22c) to see if itself is composed by other local scale-invariant sub-regions. Figure 26 shows the iso-contours of Q_ω in red and Q_s in yellow corresponding to 15% of their maximum value in this sub-region. Three different clusters were identified based on the structures seen in this figure. The structures size in the streamwise direction are approximately 200η which is of the order of magnitude of the integral length scale ($L \approx 270\eta$). For each of those structures, the second order structure function is calculated and presented in figure 27. The Kolmogorov velocity and length scales which were used to normalize the structure function are also conditioned on each cluster. The conditioning on each cluster is made by averaging the second order structure function within a rectangular prism which contains the structures seen in figure 26.

Each cluster has a different power law associated with it. Cluster A shows a 1 power law, B a 2/3 power law and C a 2/5 one. This shows that the sub-regions where the power laws were estimated in figure 23 can be themselves decomposed into smaller regions with their own power law exponents. This behaviour prompt us to reduce the size of the sub-regions and perform the same slope search as in section 5.2. This is slightly different than conditioning to specific structures as seen in figure 26. In this case the sub-region

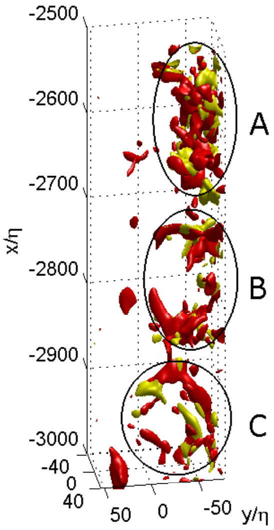

FIGURE 26. Iso-surfaces of Q_ω in red and Q_s in yellow corresponding to 15% of their respective maximum value in the sub-region $-3050 < x/\eta < -2550$ of x/x_*^{peak}=0.57.

comprises the whole domain in the yz plane in order to systematically sample the population of power laws present in the flow. The streamwise distance of these sub-regions is fixed to be a length below which the power law distribution does not change significantly. This length was determined by trial and error resulting in 160η for x/x_*^{peak}=0.57 and x/x_*^{peak}=0.94 and 120η for x/x_*^{peak}=2.04. Figure 28 shows the result of this procedure for x/x_*^{peak}=0.57. The range of power law exponents has increased in comparison to figure 23 where the streamwise length of the sub-regions is set to 500η. It is important to highlight that depending on how the volume is divided it is possible to find different power laws as it was shown in the structure functions in figure 27 conditioned to high enstrophy and energy dissipation structures in $-3050 < x/\eta < -2550$.

The point here has been to investigate what random subsets of the entire data give in terms of r-scalings of the second order structure function. These subsets may or may not be representative of the whole, but they are there. As mentioned before, power law exponents are not always well-defined, but sometimes they are. When they are, they can equal 2/3 and they can also widely differ from 2/3. These results should perhaps be interpreted in the context of models such as Lundgren's (Lundgren 1982) which relate the 2/3 law of the entire data to isolated events within the data which have a well-defined 2/3 law themselves. Our conclusion is that one can indeed find subsets with a 2/3 structure function scaling but that it is not clear whether these subsets are the sole cause of the 2/3 structure function scaling of the entire dataset. In particular, events with different structure functions scalings are also present and it is not clear how one should average out their effects.

6. Conclusions

An experimental study of the turbulence generated by a low-blockage space-filling fractal square grid was performed using cinematographic PIV in a water channel. Three stations were probed along the centreline streamwise direction, one in the production

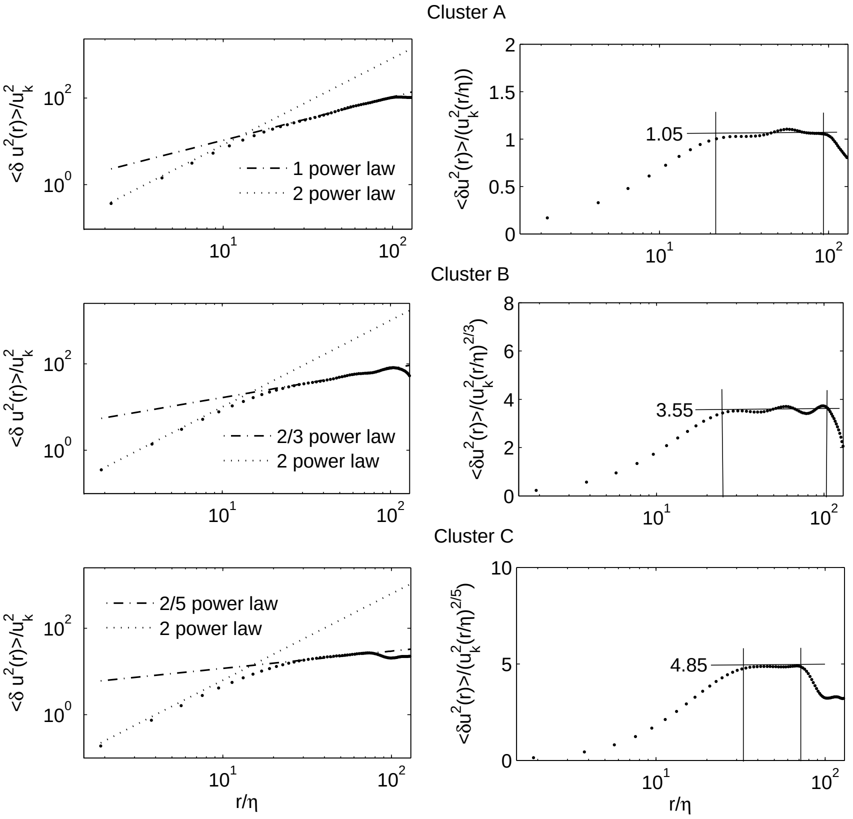

FIGURE 27. a) Second order structure function evaluated in $-3050 < x/\eta < -2550$ of x/x_*^{peak}=0.57 for the three clusters seen in figure 26 and b) the same data as in a) but compensated with $(r/\eta)^{2/3}$ and plotted in a linear-logarithmic axis. The power law plateaus seen in the linear-logarithmic axis plots are attained within a deviation of 5% and 4% from the mean values of 1.05 and 3.55 for clusters A and B, respectively. The power law plateau in cluster C has a negligible deviation when compared to the ones in A and B. The Kolmogorov velocity (u_k) and length (η) scales used to normalise the data in the figure are computed over each cluster.

region, one at the peak of turbulence intensity and one in the non-equilibrium decay region of the flow. A first result is that $\langle Q \rangle$ and $\langle R \rangle$ are very close to zero in these three stations though not quite (see figure 8).

The average production rate $\langle \omega_i s_{ij} \omega_j \rangle$ of average enstrophy and the average production rate -$\langle s_{ij} s_{jk} s_{ki} \rangle$ of average square strain rate $\langle s_{ij} s_{ji} \rangle$ decay slower in the near-field decay region than $\langle s_{ij} s_{ji} \rangle^{3/2}$. The reason for this is in the streamwise development of the asymmetric structure of the fluctuating velocity gradients which translates into changes in the distribution of the eigenvalues and in the eigenvector alignments with vorticity. Only in our decay region station are these statistics similar to the usual, perceived universal, statistics found in other flows (Tsinober 2009). Yet, this station is in the region where previous works (Seoud & Vassilicos 2007; Mazellier & Vassilicos 2010; Valente & Vassilicos 2011, 2012; Gomes-Fernandes *et al.* 2012; Discetti *et al.* 2013; Nagata *et al.* 2013) have found the non-equilibrium dissipation law $C_\epsilon \sim Re_I/Re_\lambda$. The Q-R diagram also has its usual well-developed tear-drop shape and the sign and skewed statistics of the

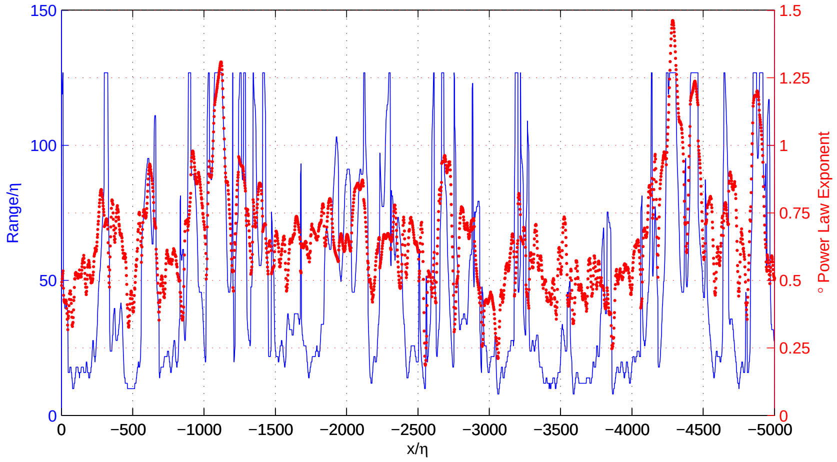

FIGURE 28. Range (continuos line) and power law p (closed circles) of the of the function $\langle \delta u^2(r) \rangle \propto r^p$. A 160η volume length in the streamwise distance was used for each x/η of the entire reconstructed volume at x/x_*^{peak}=0.57.

intermediate strain rate eigenvalue λ_2 is as reported for other flows in our non-equilibrium decay station. This leads us to conclude that the non-equilibrium decay dynamics must mostly translate in the Reynolds number scalings of the fluctuating velocity gradient statistics, less so in the flow topology implied by these statistics.

In our production region station and at the peak location, vortex stretching only slightly dominates over compression (whereas it has its usual strong statistical dominance in our decay region station). The PDFs of $\langle \omega_i s_{ij} \omega_j \rangle / \langle s_{ij} s_{ji} \rangle^{3/2}$ and of λ_2 are approximately symmetric in these stations with very much wider tails than in our decay station. Furthermore, the PDFs of λ_1 and of λ_3 closely mirror each other and also have very wide tails (very well fitted by exponentials in the production region) whereas they do not in the decay station (however these PDFs in the decay region also have well-defined exponential tails). The statistics also suggest a more balanced distribution between vortex tubes and vortex sheets (as interpreted from the sign of λ_2) in the production region and peak stations than in the decay station. Nevertheless, the 2/3 power-law dependence of the second order structure function on two-point separation is not only present in our decay station (where the streamwise fluctuating velocity component is gaussian) but also at the peak location (where it is not).

At our production region station the second order structure function does not have a well-defined 2/3 power-law shape and the streamwise fluctuating velocity component is strongly non-gaussian. However there are subsets of the overall data set in that station where very clear 2/3 power-law exponents exist defined over a wide range of two-point separations. One might have thought that the Q-R diagram in these subregions would be close to the universal tear-drop shape but it is not and its shape is nearly exactly the same as for the entire data set at this station.

We would like to express our gratitude to Oliver Buxton for providing the alignment data of the jet. We gratefully acknowledge the financial support from EPSRC through Grant No. EP/H030875/1. We also acknowledge Roland Hutchins, Ian James and Jon

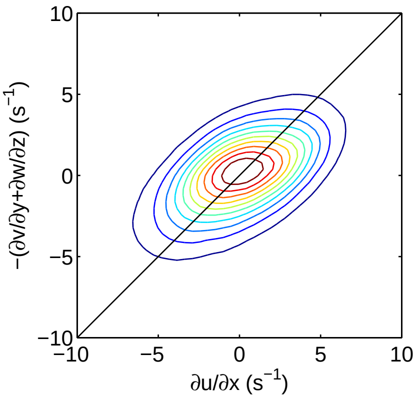

FIGURE 29. Joint PDF between $\partial u/\partial x$ and $-(\partial v/\partial y + \partial w/\partial z)$ at $x/x_*^{peak} = 2.04$. The countours range form 10^{-2} to 10^{-4}.

Cole of the Department of Aeronautics workshop for all their help with setting up the experiments.

Appendix A. Assessment of measurement accuracy

In terms of the velocity vectors, the particle displacement on each camera was, on average, around 6 pixels. This value of pixel displacement is slightly lower than usually recommended because the laser light sheet is set perpendicular to the flow and the time between pulses has to be small enough to capture the same particle in two consecutive frames. Peak locking was checked and is not presented as a problem given the high diffraction limited particle diameter caused by the high f#.

The accuracy of the velocity gradients is assessed by computing the divergence of the velocity field, $\nabla.\mathbf{u}$, which, for incompressible flows, is zero. The results presented in this sub-section are related to $x/x_*^{peak} = 2.04$ for brevity. Qualitatively there is no difference between the divergence error behaviour in this station when compared to the other stations.

Figure 29 shows the contour of the joint PDF of $\partial u/\partial x$ and $-(\partial v/\partial y + \partial w/\partial z)$. Theoretically all data should collapse in the 45° line if $\nabla.\mathbf{u} = 0$. The contours show that there is evidence of divergence error in the data. The correlation coefficient between $\partial u/\partial x$ and $-(\partial v/\partial y + \partial w/\partial z)$ is computed to be $C_T = 0.5$ for x/x_*^{peak}=0.57 and x/x_*^{peak}=0.94 and $C_T = 0.6$ for x/x_*^{peak}=2.04. The values of C_T are lower than those of Ganapathisubramani *et al.* (2007) ($C_T = 0.82$) and Tsinober *et al.* (1992) ($C_T \approx 0.7$).

Another way of quantifying the divergence error is to look at the PDF of $\nabla.\mathbf{u}$ normalized by the norm of the gradient tensor, $(\nabla\mathbf{u} : \nabla\mathbf{u})^{1/2}$. In figure 30 the distribution of the divergence error is close to a normal curve with a zero mean and a r.m.s. of 0.33 for $x/x_*^{peak} = 2.04$. At x/x_*^{peak}=0.57 and 0.94 the r.m.s. is 0.41 and 0.38, respectively. Mullin & Dahm (2006), Khashehchi *et al.* (2010) and Ganapathisubramani *et al.* (2007) reported values of 0.35, 0.3 and 0.25, respectively.

It is useful to look at how the PIV errors vary with the velocity gradient magnitude. Figure 31 shows that high magnitude gradients are correlated with lower divergence error. This behaviour will be useful when conditioning the results to more active regions of the flow where high values of dissipation or vorticity are present.

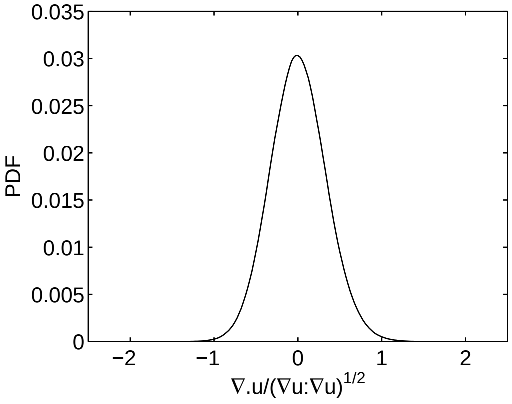

FIGURE 30. PDF of $\nabla.\mathbf{u}/(\nabla\mathbf{u}:\nabla\mathbf{u})^{1/2}$ at $x/x_*^{peak} = 2.04$. The r.m.s. of this distribution is 0.33.

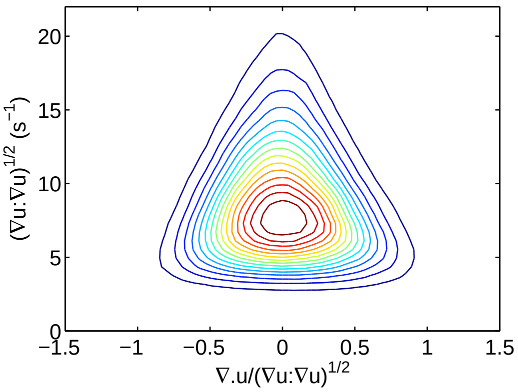

FIGURE 31. Joint PDF of $\nabla.\mathbf{u}/(\nabla\mathbf{u}:\nabla\mathbf{u})^{1/2}$ and $(\nabla\mathbf{u}:\nabla\mathbf{u})^{1/2}$ at $x/x_*^{peak} = 2.04$. Contours range from 10^{-2} to 10^{-4}.

REFERENCES

ASHURST, W. T., KERSTEIN, A. R., KERR, R. M. & GIBSON, C. H. 1987 Alignment of vorticity and scalar gradient with strain rate in simulated navier-stokes turbulence. *Phys. Fluids* **30**, 2343–2353.

BATCHELOR, G. K. 1953 *The Theory of Homogeneous Turbulence*. Cambridge Univ. Press., Cambridge.

BETCHOV, R. J. 1956 An inequality concerning the production of vorticity in isotropic turbulence. *J. Fluid Mech.* **1**, 497–504.

BETCHOV, R. J. 1975 Numerical simulation of isotropic turbulence. *Phys. Fluids* **18**, 1230–1236.

BLACKBURN, H. M., MANSOUR, N. N. & CANTWELL, B. J. 1996 Topology of fine-scale motions in turbulent channel flow. *J. Fluid Mech.* **310**, 269–292.

BUXTON, O. R. H. & GANAPATHISUBRAMANI, B. 2010 Amplification of enstrophy in the far field of an axisymmetric turbulent jet. *J. Fluid Mech.* **651**, 483–502.

BUXTON, O. R. H., LAIZET, S. & GANAPATHISUBRAMANI, B. 2011 The effects of resolution and noise on kinematic features of fine-scale turbulence. *Exp. Fluids* **51**, 1417–1437.

CANTWELL, B. J. 1992 Exact solution of a restricted euler equation for the velocity gradient tensor. *Phys. Fluids A* **4**, 782.

CHACIN, J. M. & CANTWELL, B. J. 2000 Dynamics of a low Reynolds number turbulent boundary layer. *J. Fluid Mech.* **404**, 87–115.

Chong, M. S., Soria, J., Perry, A. E., Chacin, J., Cantwell, B. J. & Na, Y. 1998 Turbulence structures of wall-bounded shear flows found using dns data. *J. Fluid Mech.* **357**, 225–247.

Dennis, D. J. C. & Nickels, T. B. 2011 Experimental measurement of large-scale three-dimensional structures in a turbulent boundary layer. Part 1. Vortex packets. *J. Fluid Mech.* **673**, 180–217.

Discetti, S., Ziskin, I. B., Astarita, T., Adrian, R. J. & Prestridge, K. P. 2013 PIV measurements of anisotropy and inhomogeneity in decaying fractal generated turbulence. *Fluid Dynamics Research* **45** (6), 061401.

van Doorne, C. W. H. & Westerweel, J. 2007 Measurement of laminar, transitional and turbulent pipe flow using stereoscopic-piv. *Exp. Fluids* **42**, 259–279.

Gamba, M., Clemens, N. T. & Ezekoye, O. A. 2013 Volumetric PIV and 2D OH PLIF imaging in the far-field of a low reynolds number nonpremixed jet flame. *Meas. Sci. Technol.* **24**, 024003.

Ganapathisubramani, B., Lakshminarasimhan, K. & Clemens, N. T. 2007 Determination of complete velocity gradient tensor by using cinematographic stereoscopic PIV in a turbulent jet. *Exp. Fluids* **42**, 923–939.

Ganapathisubramani, B., Lakshminarasimhan, K. & Clemens, N. T. 2008 Investigation of three-dimensional structure of fine scales in a turbulent jet by using cinematographic stereoscopic particle image velocimetry. *J. Fluid Mech.* **598**, 141–175.

Gomes-Fernandes, R., Ganapathisubramani, B. & Vassilicos, J. C. 2012 Particle image velocimetry study of fractal-generated turbulence. *J. Fluid Mech.* **711**, 306–336.

Gulitski, G., Kholmyansky, M., Kinzelbach, W., Lüthi, B., Tsinober, A. & Yorish, S. 2007 Velocity and temperature derivatives in high-Reynolds-number turbulent flows in the atmospheric surface layer. Part 1. Facilities, methods and some general results. *J. Fluid Mech.* **589**, 57–82.

Hurst, D. & Vassilicos, J. C. 2007 Scalings and decay of fractal-generated turbulence. *Phys. Fluids* **19** (035103).

Jayesh & Warhaft, Z. 1992 Probability distribution, conditional dissipation, and transport of passive temperature fluctuations in grid-generated turbulence. *Phys. Fluids A* **4**, 2292–2307.

Khashehchi, M., Elsinga, G. E., Ooi, A., Soria, J. & Marusic, I. 2010 Studying invariants of the velocity gradient tensor of a round turbulent jet across the turbulent/nonturbulent interface using tomo-piv. In *Proceedings of the 15th International Symposium on Applications of Laser Techniques to Fluid Mechanics 2010*. Springer Verlag.

Kholmyansky, M. & Tsinober, A. 2009 On an alternative explanation of anomalous scaling and how well-defined is the concept of inertial range. *Phys. Lett. A* **373** (27), 2364–2367.

Kholmyansky, M., Tsinober, A. & Yorish, S. 2001 Velocity derivatives in the atmospheric surface layer at $Re_\lambda = 10^4$. *Phys. Fluids* **13**, 311–314.

Kolmogorov, A. N. 1941*a* Dissipation of energy in locally isotropic turbulence. *C.R. Akad Sci. SSSR* **32**, 16–18.

Kolmogorov, A. N. 1941*b* The local structure of turbulence in incompressible viscous fluid for very large reynolds numbers. *C.R. Akad Sci. SSSR* **30**, 301–305.

Kolmogorov, A. N. 1941*c* On degeneration of isotropic turbulence in an incompressible viscous liquid. *C.R. Akad Sci. SSSR* **31**, 538–540.

Krogstad, P.Å. & Davidson, P. A. 2012 Near-field investigation of turbulence produced by multi-scale grids. *Phys. Fluids* **24** (3), 035103.

Laizet, S., Vassilicos, J. C. & Cambon, C. 2013 Interscale energy transfer in decaying turbulence and vorticity-strain rate dynamics in grid-generated turbulence. *Fluid Dynamics Research* **45** (6), 061408.

Lundgren, T. S. 1982 Strained spiral vortex model for turbulent fine structure. *Phys. Fluids* **25** (12), 2193–2203.

Lüthi, B., Tsinober, A. & Kinzelbach, W. 2005 Lagrangian measurement of vorticity dynamics in turbulent flow. *J. Fluid Mech.* **528**, 87–118.

Mazellier, N. & Vassilicos, J. C. 2010 Turbulence without Richardson-Kolmogorov cascade. *Phys. Fluids* **22** (075101).

Mouri, H., Hori, A. & Takaoka, M. 2008 Fluctuations of statistics among subregions of a turbulence velocity field. *Phys. Fluids* **20** (035108).

Mullin, J. A. & Dahm, W. J. A. 2006 Dual-plane stereo particle image velocimetry measurements of velocity gradient tensor fields in turbulent shear flow. i. accuracy assessments. *Phys. Fluids* **18** (035101).

Nagata, K., Sakai, Y., Suzuki, H., Suzuki, H., Terashima, O. & Inaba, T. 2013 Turbulence structure and turbulence kinetic energy transport in multiscale/fractal-generated turbulence. *Phys. Fluids* **25** (065102).

Ooi, M. A., Soria, J. & Chong, M. 1999 A study of the evolution and characteristics of the invariants of the velocity-gradient tensor in isotropic turbulence. *J. Fluid Mech.* **381**, 141–174.

Prasad, A. K. & Jensen, K. 1995 Scheimpflug stereocamera for particle image velocimetry in liquid flows. *Appl. Opt.* **34** (30), 7092–7099.

Raffel, M. 2007 *Particle image velocimetry: a practical guide*. Springer.

Seoud, R. E. & Vassilicos, J. C. 2007 Dissipation and decay of fractal-generated turbulence. *Phys. Fluids* **19** (105108).

Simmons, L. F. G. & Salter, C. 1934 Experimental investigation and analysis of the velocity variations in turbulent flow. *Proc. Roy. Soc. A* **145** (854), 212–234.

Soloff, S. M., Adrian, R. J. & Liu, Z-C. 1997 Distortion compensation for generalized stereoscopic particle image velocimetry. *Meas. Sci. Technol.* **8**, 1441–1454.

Soria, J., Sondergaard, R., Cantwell, B. J., Chong, M. S. & Perry, A. E. 1994 A study of the fine-scale motions of incompressible time-developing mixing layers. *Phys. Fluids* **6**, 871–884.

Sreenivasan, K. R. & Antonia, R. A. 1997 The phenomenology of small-scale turbulence. *Ann. Rev. Fluid Mech.* **29** (1), 435–472.

Steinberg, A. M., Driscoll, J. F. & Ceccio, S. L. 2008 Measurements of turbulent premixed flame dynamics using cinema stereoscopic piv. *Exp. Fluids* **44**, 985–999.

Taylor, G. I. 1938 Production and dissipation of vorticity in a turbulent fluid. *Proc. Roy. Soc. A* **164**, 15–23.

Tennekes, H. & Lumley, J. L. 1972 *A first course in turbulence*. MIT Press, Cambridge, Mass.

Tsinober, A. 2000 Vortex stretching versus production of strain/dissipation. *Turbulence Structure and Vortex Dynamics* pp. 164–191.

Tsinober, A. 2009 *An informal conceptual introduction to turbulence*. New York: Springer.

Tsinober, A., Eggels, J. G. M. & Nieuwstadt, F. T. M. 1995*a* On alignments and small scale structure in turbulent pipe flow. *Fluid Dynamics Research* **16** (5), 297–310.

Tsinober, A., Kit, E. & Dracos, T. 1992 Experimental investigation of the field of velocity gradients in turbulent flows. *J. Fluid Mech.* **242**, 169–192.

Tsinober, A., Shtilman, L., Sinyavskii, A. & Vaisburd, H. 1995*b* Vortex stretching and enstrophy generation in numerical and laboratory turbulence. In *Small-Scale Structures in Three-Dimensional Hydrodynamic and Magnetohydrodynamic Turbulence*, pp. 9–16. Springer.

Valente, P. C. & Vassilicos, J. C. 2011 The decay of turbulence generated by a class of multi-scale grids. *J. Fluid Mech.* **687**, 300–340.

Valente, P. C. & Vassilicos, J. C. 2012 Universal dissipation scaling for non-equilibrium turbulence. *Phys. Rev. Lett.* **108**, 214503.

Westerweel, J. 1993 *Digital particle image velocimetry*. Delft: Delft University Press.

Yanitskii, V. E. 1982 Transport equation for the deformation-rate tensor and description of an ideal incompressible liquid by a system of equations of the dynamical type. *Sov. Phys. Dokl.* **27**, 701.